The International Joint Virtual Conferences Surfaces, Coatings and Interfaces

SurfCoat Korea 2021

&

Graphene Korea 2021

Held Virtually - May 26 to 28, 2021

Conference Proceedings

DOI: https://doi.org/10.26799/cp-surfcoat-graphene-korea-2021

Proceedings of the SurfCoat Korea 2021 / Graphene Korea 2021 Joint Virtual International Conferences
May 26 – 28, 2021, (Held Virtually)
DOI: https://doi.org/10.26799/cp-surfcoat-graphene-korea-2021

Photoluminescence and structural defects of ZnO films deposited by reactive magnetron sputtering with unconventional Ar-O_2 gas mixture formation

Kristina Bockute[1], Emilija Demikyte[2], Simona Tuckute[3], Marius Urbonavicius[4], Sarunas Varnagiris[5], Giedrius Laukaitis[6], Martynas Lelis[7]

[1]Kaunas University of Technology, K. Donelaičio st. 73, Kaunas, Lithuania, kristina.bockute@ktu.lt
[2]Vytautas Magnus University, K. Donelaičio st. 58, Kaunas, Lithuania, emilija.demikyte@alumni.vdu.lt
[3]Lithuanian Energy Institute, Breslaujos st. 3, Kaunas, Lithuania, simona.tuckute@lei.lt
[4]Lithuanian Energy Institute, Breslaujos st. 3, Kaunas, Lithuania, marius.urbonavicius@lei.lt
[5]Lithuanian Energy Institute, Breslaujos st. 3, Kaunas, Lithuania, sarunas.varnagiris@lei.lt
[6]Kaunas University of Technology, K. Donelaičio st. 73, Kaunas, Lithuania, giedrius.laukaitis@ktu.lt
[7]Lithuanian Energy Institute, Breslaujos st. 3, Kaunas, Lithuania, martynas.lelis@lei.lt

Abstract

ZnO is a well-known traditional industrial material which has high potential to become one of the key components for the next generation of future electronics, LED emitters, visible light photocatalysis and others. In its pristine form ZnO has relatively wide band gap of approximately 3.4 eV, but a lot of emerging applications requires some level of electronic structure engineering and structure optimisation. Studies show that ZnO properties strongly depend on the intrinsic defects type and concentrations. Both characteristics usually are depending on the synthesis method. Accordingly, there is great interest to develop new methods which would allow to obtain ZnO with optimised band gap and other properties. In current, study ZnO films were deposited using reactive magnetron sputtering with unconventional Ar-O_2 gas mixture supply control: Ar flow was controlled to maintain total gas pressure at $1x10^{-2}$ mbar, whereas O_2 flow rate was actively adjusted to maintain the selected intensity of optical zinc emission from the working cathode zone. Applying such ZnO formation method it was possible to stabilise reactive magnetron sputtering process over wide range of conditions. Elemental composition analysis by XPS revealed that despite large variations in Zn emission peak intensity within tested experimental conditions all films had nearly identical Zn:O ratios but at the same time their structural and optical properties differed significantly. The colour of the films varied from highly transparent yellowish-greenish, to intense orange, to opaque black. XRD analysis showed that films consisted of single polycrystalline wurtzite phase with varying orientations. PL spectroscopy analysis revealed that films had a lot of various defects including oxygen and zinc vacancies, interstitials and surface defects. Wide variation of ZnO properties obtained by different reactive sputtering conditions demonstrates the potential of the proposed method to control the formation of various intrinsic defects and to tailor their concentration.

Keywords: ZnO films, reactive magnetron sputtering, photoluminescence, structural defects, energy levels, optical properties.

1. Introduction

ZnO has an intriguing set of properties: direct wide band gap of 3.44 eV at low temperatures and approximately 3.3 eV at room temperature [1], [2]; relatively large exciton binding energy of approximately 60 meV [3], [4]; strong piezoelectric and pyroelectric properties [5]; intensive luminescence in the visible light spectra [6], [7]; strong sensitivity of surface conductivity to interaction with surrounding liquids and gases [8]; non-linear electrical resistance [9]; second- and third- order non-linear optical properties [10]; high thermal conductivity [11], [12], etc. Exploitation of these properties already made ZnO an important industrial material which is widely used in numerous applications starting from additives to rubber matrix [11] to improve its thermal conductivity or as main functional

material in varistors [9] and finishing with various advanced optical and semiconductor-based technologies [13].

As semiconductor ZnO is quite similar to the more established GaN [14]. Unfortunately, up to now ZnO still suffers from several issues which were already successfully solved for GaN. Probably the biggest challenges (and opportunities) are related to the ability to reliably produce stable p-type ZnO in bulk or film form [15]. This issue is potentially strongly related to the peculiarities of ZnO structure and its tendency to form native or intrinsic defects [14]. More recently, it was shown that type and prevalence of intrinsic defects is strongly related to the specific ZnO synthesis methods and that they might be acting to compensate some other features of the structure (for example intentional or unintentional doping). Accordingly, there is still a lot of efforts to find new or improved ZnO synthesis methods which would open up wide possibilities to form p-n junctions, and to use other semiconductor engineering techniques to produce ZnO based laser, LEDs, photocatalytic devices, etc [15].

During our previous study [16] we demonstrated that it is possible to use reactive magneton sputtering with unconventional gas phase composition control method and to stabilise ZnO film formation in between "pure" oxide and "pure" metallic phases. In current study we further examine the possibilities of the proposed gas phase control method and provide more details on the specific structural and optical characteristics of ZnO films.

2. Methodology

2.1. Film deposition

All investigated ZnO films were deposited by magnetron sputtering performed at custom modified PVD-75 physical vapor deposition system (Kurt J. Lesker Company) equipped with cryogenic vacuum pump. Ultimate vacuum pressure prior to each experiment was at least $1x10^{-7}$ mbar. Sputtering was conducted using one Torrus 3 magnetron with metallic Zn disk (76 mm diameter, 99.99 % purity) as primary cathode material (sputtering target). Magnetron was powered by Kurt J. Lesker R301 radio frequency (RF) power supply working at experimentally preselected 150 W power level. Films were deposited on borosilicate glass discs (diameter - 30 mm) which have high transparency in visible and near-UV spectra.

In our previous study [16] we demonstrated that RF magnetron sputtering of Zn target in reactive Ar:O_2 atmosphere using fixed Ar:O_2 gas flow ratios has a tendency to a) poison Zn target surface by oxygen and to switch to ZnO oxide deposition mode; or b) to clean Zn target from oxygen and to switch to metallic Zn film (with some oxygen impurities) deposition mode. The transitional range of Ar:O_2 gas flow ratio between oxide and metallic film deposition modes was relatively narrow and had strong hysteresis, therefore film deposition in this region was unstable and their properties were not repeatable.

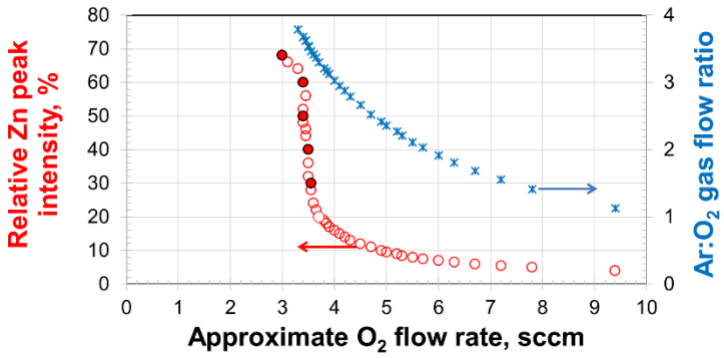

Fig. 1: Relationship between relative Zn emission intensity, O_2 flow rate and Ar:O_2 gas flow rate ratio.

In order to stabilize deposition process inside this narrow transitional range an alternative O_2 and Ar gas supply method was developed. By this method Ar Mass Flow Controller (MFC) was connected to the vacuum meter and controlled to maintain total pressure constant at $1x10^{-2}$ mbar. At the same time independently from the argon supply, oxygen MFC was connected to the interface of optical spectrometer (Flotron X, Nova Fabrica Ltd) whose feedback signal was used to maintain the selected

intensity level of Zn emission peak from plasma above Zn target in 478-480 nm spectral range. This approach has proven to provide reasonable magnetron sputtering process stabilization inside the transition region, although Ar:O_2 MFC flow rate ratio changed faintly (Fig. 1).

For current study, ZnO samples were synthesized maintaining relative Zn peak intensity at 30, 40, 50, 60 and 68 % (for the simplicity in the following text samples will be named only by the percentage of the corresponding relative Zn peak intensity). Sample deposition rates had nearly linear dependence on relative Zn intensity (Fig. 2) and varied between approximately 32 and 115 nm/min. Accordingly, during fixed 60 min deposition time reactive magnetron sputtering produced films with thickness ranging from approximately 1900 nm up to nearly 7000 nm,

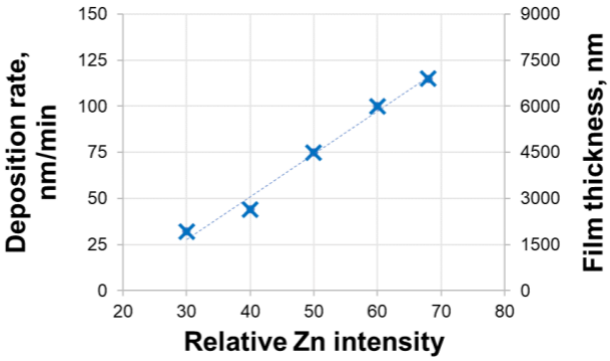

Fig. 2: Deposition rates and sample thickness obtained using different relative Zn emission intensities.

2.2. Film characterisation

Crystal structure of deposited films was investigated by X-ray diffractometer (Bruker D8) operating with Cu Kα radiation. Surface microstructure of the films was analysed by Scanning Electron Microscope (Hitachi S-3400N). Optical transmittance of the films was measured using UV–Visible–near-IR spectrophotometer (Jasco V-650) at normal incidence from 350 nm to 800 nm. Band gap values were calculated from the Tauc plots. Elemental composition was estimated using XPS (PHI 5000 Versaprobe) with Ar+ ion pre-sputtering. PL spectroscopy measurements was performed using Edinburgh Instruments FLS980 instrument with 340 nm excitation source.

3. Results and discussions

Traditionally ZnO films deposited by RF magnetron sputtering in oxygen rich gas mixtures form wurtzite crystal structure [17] which appears transparent and nearly colourless or has only light yellowish-greenish shade. In current study 30 % and 40 % samples matched those traditional characteristics of commonly observed ZnO films: deposited films had characteristic shade (Fig. 3) and their optical transmission reached up to 80-90 % (Fig. 4).

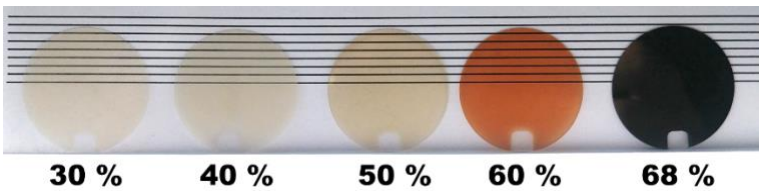

Fig. 3. Visual appearance of ZnO films.

By increasing Zn peak intensity (i.e. by reducing partial oxygen pressure) tone of the films got darker and their optical transmission decreased significantly. Eventually, films deposited using largest Zn emission intensity were almost black with nearly no transmission in whole visible light spectra. It can be noticed that reduction of optical transmission of the films is not uniform and is stronger at the lower wavelengths than at the higher end of the spectrum. Moreover, darkening of the films is accompanied by the shift of the absorption edge to higher wavelengths and corresponding reduction of the band gap from 3.22 eV to 3.06-3.08 eV.

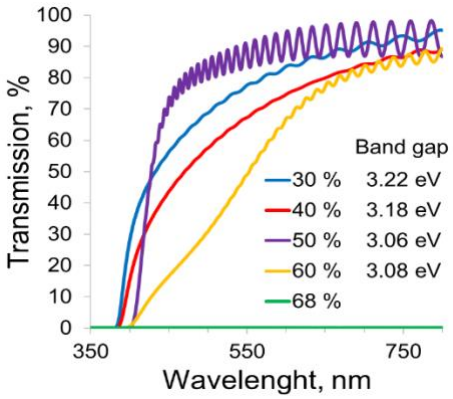

Fig. 4. Optical transmission spectra and band gap values of ZnO films.

Interestingly, the lowest band gap values were observed for 50 % and 60 % samples which have significantly different optical and structural characteristics. 60 % sample has intense orange colour which is quite typical for the natural ZnO mineral – zincite [18], but up to our knowledge was never reported for the ZnO films produced by magnetron sputtering. The possibility of observation of zincite phase is also indirectly rejected by the mismatch between reported band gap of zincite which is approximately 3.2 eV [19] and experimentally observed value of 3.08 eV. Also, the presence of zincite phase is not confirmed by XRD (Fig. 5) which shows that 60 % sample has the same wurtzite ZnO phase as all other samples. On the other hand, despite the presence of only one crystal phase (namely wurtzite ZnO), XRD patterns reveal that between the samples there are some noticeable differences in their crystallinity and even more pronounced discrepancies in their orientation distribution.

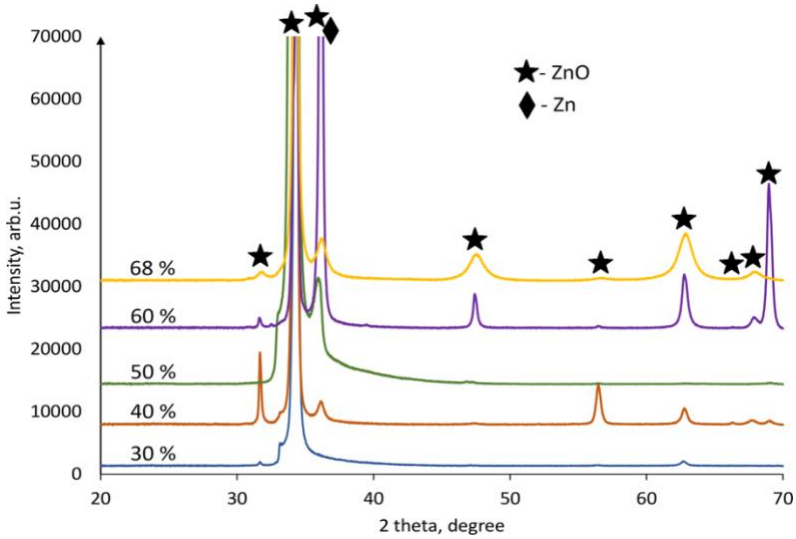

Fig. 5. XRD patterns of ZnO films

Starting from the 30 % sample, one can see that it has highly crystalline ZnO phase with totally dominating (002) orientation. (002) plane (at approximately 34.5°) of wurtzite ZnO has the lowest surface free energy [20] and it is observed by almost all researchers who perform magnetron sputter deposition of undoped ZnO films. When film deposition is performed using higher Zn peak intensities (i.e. lower partial O_2 pressures), new crystalline orientations emerge: (100) at approximately 31.8°; (101) at 36.4°; (102) at 47.6°; (110) at 56.7°; (103) at 63.1°; (112) at 68.1° and (201) at 69°. Interestingly, 60 % and 68 % samples both have polycrystalline structure with generally similar orientation distribution, but this distribution is much different from the 40 % sample which also has several strongly expressed orientations, but their relative intensity distribution is significantly different. More specifically 40 % sample has strongly expressed (101) and (103) planes which are quite weak in 50 %, 60 % and 68 % samples.

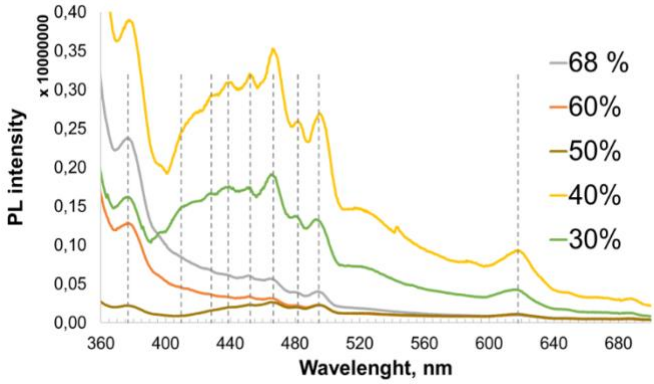

Fig. 6. PL spectra of ZnO films. Main peaks are attributed to following transitions reported in literature [1]: CB-VB (375-380 nm), CB-V_{Zn} (408 nm), CB-O_i (428 nm), Zn_i-V_{Zn} (437 nm), surface defects of ZnO (451 nm and 483 nm), CB-V_O (515 nm).

XPS elemental composition analysis revealed that all samples have oxygen concentration of 42.1-42.4 at. % and Zn concentration of 57.6-57.9 at. %. No significant variation in Zn:O ratio (all concentration variations were random and did not exceeded typical XPS error) and relatively strong variation in preferred crystal plane orientation suggests that reactive magnetron sputtering process with unconventional gas phase control method allowed to introduce subtle changes in ZnO microstructure. PL spectroscopy data (Fig. 6) confirms such assumption and indicates that most of the discrepancies between the samples can be related to the different concentrations and/or type of intrinsic defects. For instance, 30 % and 40 % samples probably had all types of possible intrinsic defects and consequently had relatively strong PL radiation with numerous peaks placed mostly at the low end of the visible light spectra. 50 %, 60 % and 68 % samples had considerably less PL peaks and suggested more homogeneous and better ordered structure of the films. In this respect, we would like to pay special attention to 50 % sample. This sample had the smallest band gap value, but at the same time it had the steepest adsorption edge, the most uniform light transmission over all visible light spectrum and the smallest intensity of PL peaks which could be attributed to intrinsic defects. Moreover, it had relatively uniform surface microstructure consisting from small (approximately 1 μm in diameter) pyramidic formations (Fig. 7), meanwhile SEM images of other samples surfaces revealed that they had considerably larger and, in most cases, non-uniformly shaped formations.

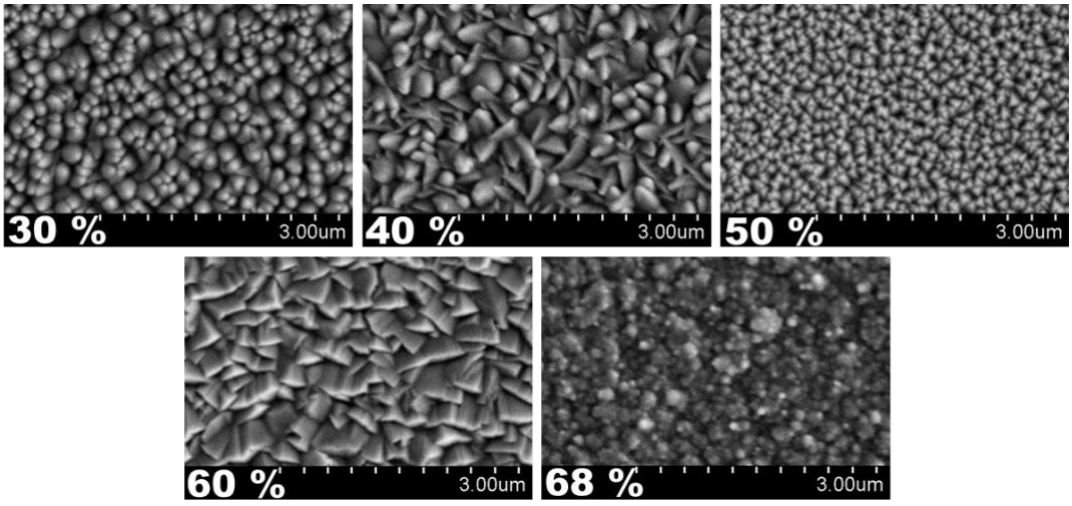

Fig. 7. SEM images of ZnO film surfaces

4. Conclusions

In current study ZnO films were deposited by reactive magnetron sputtering technique with unconventional control of the Ar-O_2 working gas mixture supply. Elemental composition analysis by

XPS revealed that all tested films had nearly identical Zn:O ratios but at the same time their structural and optical properties differed significantly. The colour of the films varied from highly transparent yellowish-greenish, to intense orange, to opaque black. XRD analysis showed that films consisted of single polycrystalline Wurtzite ZnO phase with varying orientations. PL spectroscopy analysis revealed that films had a lot of various defects including oxygen and zinc vacancies as well as their interstitials and surface defects. Wide variation of ZnO properties obtained by different reactive sputtering conditions demonstrates the potential of the proposed method and opens up new possibilities to control the formation of various intrinsic defects and to tailor their concentration.

Acknowledgements

This research is funded by the European Social Fund according to the activity 'Improvement of researchers' qualification by implementing world-class R&D projects' of Measure No. 09.3.3-LMT-K-712, project "Investigation of the application of TiO_2 and ZnO for the visible light assisted photocatalytical disinfection of the biologically contaminated water" (09.3.3-LMT-K-712-01-0175).

References

[1] A. Mang, K. Reimann, and S. Rübenacke, "Band gaps, crystal-field splitting, spin-orbit coupling, and exciton binding energies in ZnO under hydrostatic pressure," *Solid State Commun.*, vol. 94, no. 4, pp. 251–254, 1995, doi: https://doi.org/10.1016/0038-1098(95)00054-2.

[2] A. Saboor, S. M. Shah, and H. Hussain, "Band gap tuning and applications of ZnO nanorods in hybrid solar cell: Ag-doped verses Nd-doped ZnO nanorods," *Mater. Sci. Semicond. Process.*, vol. 93, pp. 215–225, 2019, doi: https://doi.org/10.1016/j.mssp.2019.01.009.

[3] D. C. Reynolds, D. C. Look, and B. Jogai, "Optically pumped ultraviolet lasing from ZnO," *Solid State Commun.*, vol. 99, no. 12, pp. 873–875, 1996, doi: https://doi.org/10.1016/0038-1098(96)00340-7.

[4] D. M. Bagnall *et al.*, "Optically pumped lasing of ZnO at room temperature," *Appl. Phys. Lett.*, vol. 70, no. 17, pp. 2230–2232, Apr. 1997, doi: 10.1063/1.118824.

[5] G. Clementi, S. Margueron, M. A. Suarez, T. Baron, B. Dulmet, and A. Bartasyte, "Piezoelectric and Pyroelectric Energy Harvesting from Lithium Niobate Films," *J. Phys. Conf. Ser.*, vol. 1407, p. 12039, 2019, doi: 10.1088/1742-6596/1407/1/012039.

[6] Y. Ma *et al.*, "Charge transfer-induced photoluminescence in ZnO nanoparticles," *Nanoscale*, vol. 11, no. 18, pp. 8736–8743, 2019, doi: 10.1039/C9NR02020A.

[7] S. Vempati, J. Mitra, and P. Dawson, "One-step synthesis of ZnO nanosheets: A blue-white fluorophore," *Nanoscale Res. Lett.*, vol. 7, pp. 1–10, 2012, doi: 10.1186/1556-276X-7-470.

[8] O. Schmidt *et al.*, "Analysis of a conducting channel at the native zinc oxide surface," *Superlattices Microstruct.*, vol. 39, no. 1, pp. 8–16, 2006, doi: https://doi.org/10.1016/j.spmi.2005.08.056.

[9] T. K. Gupta, "Application of Zinc Oxide Varistors," *J. Am. Ceram. Soc.*, vol. 73, no. 7, pp. 1817–1840, Jul. 1990, doi: https://doi.org/10.1111/j.1151-2916.1990.tb05232.x.

[10] M. C. Larciprete, D. Haertle, A. Belardini, M. Bertolotti, F. Sarto, and P. Günter, "Characterization of second and third order optical nonlinearities of ZnO sputtered films," *Appl. Phys. B*, vol. 82, no. 3, pp. 431–437, 2006, doi: 10.1007/s00340-005-2022-z.

[11] Q. Mu, S. Feng, and G. Diao, "Thermal conductivity of silicone rubber filled with ZnO," *Polym. Compos.*, vol. 28, no. 2, pp. 125–130, Apr. 2007, doi: https://doi.org/10.1002/pc.20276.

[12] Ü. Özgür *et al.*, "Thermal conductivity of bulk ZnO after different thermal treatments," *J. Electron. Mater.*, vol. 35, no. 4, pp. 550–555, 2006, doi: 10.1007/s11664-006-0098-9.

[13] L. Chen, J. Cui, X. Sheng, T. Xie, T. Xu, and X. Feng, "High-Performance Photoelectronic Sensor Using Mesostructured ZnO Nanowires," *ACS Sensors*, vol. 2, no. 11, pp. 1567–1572, Nov. 2017, doi: 10.1021/acssensors.7b00477.

[14] A. Janotti and C. G. Van de Walle, "Fundamentals of zinc oxide as a semiconductor," *Reports Prog. Phys.*, vol. 72, no. 12, p. 126501, 2009, doi: 10.1088/0034-4885/72/12/126501.

[15] S. Vyas, "A Short Review on Properties and Applications of Zinc Oxide Based Thin Films and Devices : ZnO as a promising material for applications in electronics, optoelectronics, biomedical and sensors," *Johnson Matthey Technology Review*, vol. 64, no. 2. pp. 202–218,

[Online]. Available: https://www.ingentaconnect.com/content/matthey/jmtr/2020/00000064/00000002/art00013.

[16] M. Lelis, S. Tuckute, S. Varnagiris, M. Urbonavicius, K. Bockute, and G. Laukaitis, "Synthesis and analysis of metallic Zn phase rich ZnO oxide films for the photocatalytic water treatment technologies," *Mater. Today Proc.*, 2020, doi: https://doi.org/10.1016/j.matpr.2020.03.197.

[17] J. Soudi, K. M. Sandeep, B. K. Sarojini, P. S. Patil, S. R. Maidur, and K. M. Balakrishna, "Thermo-optic effects mediated self focusing mechanism and optical power limiting studies of ZnO thin films deposited on ITO coated PET substrates by RF magnetron sputtering under continuous wave laser regime," *Optik (Stuttg).*, vol. 225, no. July 2020, p. 165835, 2021, doi: 10.1016/j.ijleo.2020.165835.

[18] J. W. Anthony, R. A. Bideaux, K. W. Bladh, and M. C. Nichols, "Handbook of Mineralogy," *Mineralogical Society of America, Chantilly, VA 20151-1110, USA. http://www.handbookofmineralogy.org/*. .

[19] S. K. Noukelag *et al.*, "Investigation of structural and optical properties of biosynthesized Zincite (ZnO) nanoparticles (NPs) via an aqueous extract of Rosmarinus officinalis (rosemary) leaves," *MRS Adv.*, vol. 5, no. 45, pp. 2349–2358, 2020, doi: 10.1557/adv.2020.220.

[20] S. Kunj and K. Sreenivas, "Residual stress and defect content in magnetron sputtered ZnO films grown on unheated glass substrates," *Curr. Appl. Phys.*, vol. 16, no. 7, pp. 748–756, 2016, doi: 10.1016/j.cap.2016.04.008.

Proceedings of the SurfCoat Korea 2021 / Graphene Korea 2021 Joint Virtual International Conferences
May 26 – 28, 2021, (Held Virtually)
DOI: https://doi.org/10.26799/cp-surfcoat-graphene-korea-2021

Synthesis of 5,15-A_2BC-Type Porphyrins to Modify a Field-Effect Transistor for Detection of Gram-Negative Bacteria

Laurie Neumann[1], Lea Könemund[1], Felix Hirschberg[1], Rebekka Biedendieck[2], Dieter Jahn[2], Hans-Hermann Johannes[1,*], Wolfgang Kowalsky[1]

[1]TU Braunschweig, Institut für Hochfrequenztechnik, Braunschweig, Germany
[2]TU Braunschweig, Institute of Microbiology and Braunschweig Integrated Centre of System Biology (BRICS), Braunschweig, Germany
[*] Corresponding author. E-mail: h2.johannes@ihf.tu-bs.de

Abstract

Current biological sensing technologies of bacteria are time consuming, labor intensive and thus expensive. Furthermore, their accuracy and reproducibility could be improved. Conventional electrical measurement methods might combine high sensitive sensing systems with biological requirements. A promising approach is the trapping of bacteria on the surface of the gate-electrode of a modified field-effect transistor (FET) using porphyin based self-assembled monolayers (SAMs). 5,15-A_2BC-type porphyrins were synthesized originating from a 5,15-diphenylporphyrin with the functionality to connect to a gold surface. The SAM formation on the surface of the gold electrode was proven by well-established analytical methods. In this work a synthesis route is presented for a linker which is attached to a peptide or cysteine group for trapping of Gram-negative bacteria. Fluorescence lifetime imaging microscopy (FLIM) measurements of porphyrin-stained bacteria were performed to verify the linkage ability.

Keywords: porphyrin, self-assembled monolayer (SAM), detection of Gram-negative bacteria, sensing of bacteria.

1. Introduction

Due to the fact, that more than half of the yearly infections are caused by *E. coli* (*Escherichia coli*), a fast and reliable detection method is of high interest.[1] Currently, detection methods are cell culturing, polymerase chain reaction (PCR) or enzyme-linked immunosorbent assay's (ELISA). Cell culturing or a PCR tests attain in high sensitivity, but for these methods specialized equipment and educated personnel are required and they are time consuming. Rapid detection is achieved with ELISA, but with the considerable drawback of a high error rate (so-called false-positive).[2-4] The development of a sensor for a fast, accurate, cost-effective, and highly sensitive detection despite simple handling is the aim for next generation of bacteria detection. In our contribution we present a novel bio-linker which has the ability to retain the bacterial cell on the sensor surface to avoid further sample preparation. As sensing device, a field-effect transistor (FET) is utilized which can sensitively detect changes in the current-voltage characteristics due to attached bacteria cells. The gate contact is coated with a bio-inspired porphyrin. Porphyrins are of great interest due to their biological compatibility, their fluorescence in the visible range, their chemical accessibility, and their stability. Porphyrins have already been used in various sensor systems.[5] In our work, we synthesized porphyrins with two different bio-receptors for bacteria linkage. We demonstrate that we can connect the porphyrin through this bio-receptor to *E. coli* cells by FLIM. Changes in the fluorescence lifetime of the porphyrin molecules and interactions due to changes in their chemical environment can be shown with this analytical method. In a next step these porphyrin molecules were modified with a linker group that can be connected on the gold contact to form a porphyrin self-assembled monolayer (SAM). The functionalized gold surfaces are analyzed by UV/Vis spectroscopy, Drop-Shape-Analysis (DSA), Infrared Reflection-Absorption Spectroscopy (IRRAS) and Cyclic Voltammetry (CV) to characterize SAM formation and molecule orientation. Furthermore, these SAM gold substrates are examined regarding their ability to link to 4',6-diamidino-2-phenylindole (DAPI)-stained *E. coli* cells on the surface.[6] The results are a promising step for the development of a new porphyrin modified surface for the detection of bacteria cells.

2. Results and Discussion

The porphyrins were synthesized starting from a 5,15-diphenyporphyrin (**1**), shown in scheme 1. All synthesized porphyrins were characterized by NMR spectroscopy, ESI-MS and UV/Vis absorption spectroscopy. The

porphyrins **2**-**6** were synthesized according to literature with minor changes to these published procedures.[7-12] In a last step the bioreceptors were attached to the maleimide group of the porphyrin by the sulfuric group of the bioreceptor. As one bioreceptor a cysteine group was attached to result porphyrin **7** and as the other bioreceptor the peptide with the amino acid sequence YVLWKRKRKFCFI-Amide was attached to result porphyrin **8**. For the peptide it has already been shown, that it can be connected to the outer membrane of *E. coli* cells due to its high compatibility to neutralize lipopolysaccharide.[13,14]

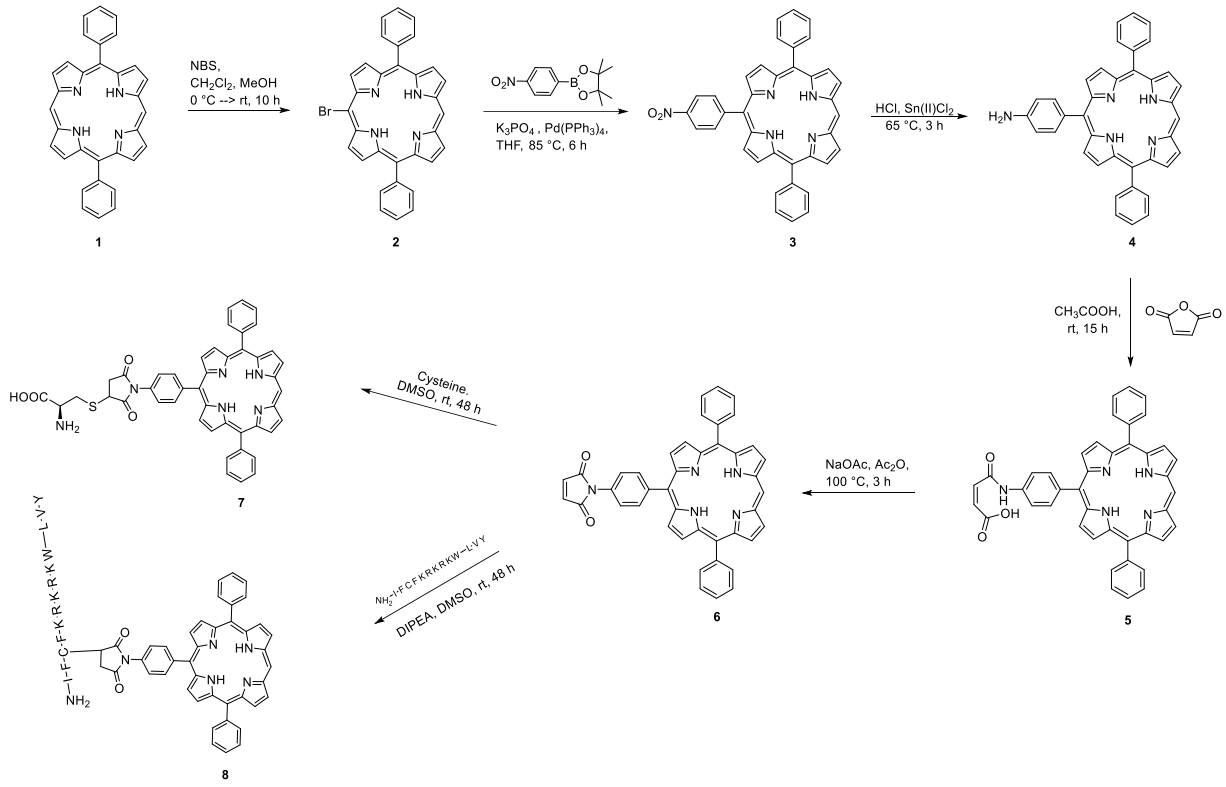

Scheme 1: Synthesis pathway with reaction conditions and reagents for the porphyrin synthesis.

The interactions of the porphyrins **7** and **8** with *E. coli* cells are analyzed by FLIM. In comparison to fluorescence microscopy, that displays the intensity of emission of the molecules, FLIM detects the fluorescence lifetime of the molecules. By this highly sensitive method, changes in the molecular environment or molecular conformations can be observed. In Figure 1 the results of the porphyrin-stained *E. coli* cells are presented. For the fluorescence lifetime of the porphyrins in the FLIM images (Figure 1) and in solution (DMSO, c = $2 \cdot 10^{-5}$ mol/L) a monoexponential decay is determined.

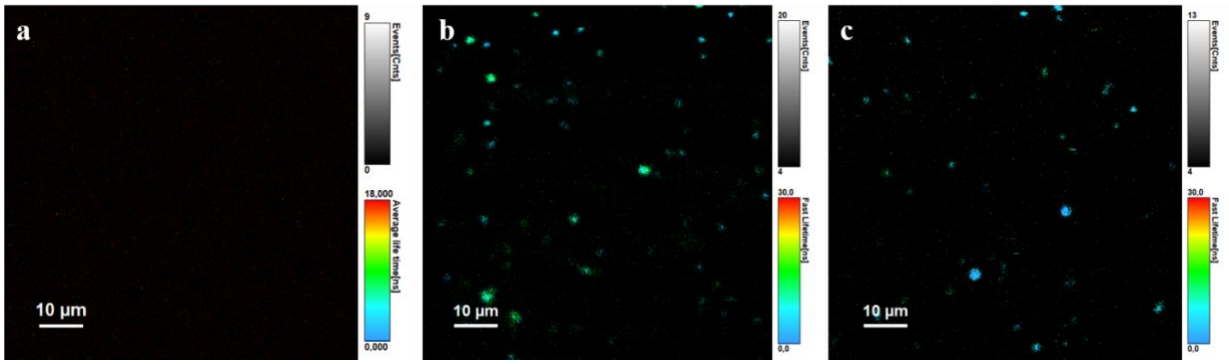

Figure 1: FLIM image at an excitation wavelength λ_{Ex} = 405 nm. (a) *E. coli* in PBS. (b) *E. coli* in PBS with Porphyrin **7**. (c) *E. coli* in PBS with Porphyrin **8**.

For porphyrin **7** the fluorescence lifetime in DMSO is derived with τ = 12.5 ns in comparison to the porphyrin-stained *E. coli* cells with τ = 6.3 ns. Here a decrease of the fluorescence lifetime τ can be observed due to

interactions with the bacteria cells. Similarly, for porphyrin **8** a decrease of τ can be observed, as the fluorescence lifetime in DMSO is determined with τ = 12.6 ns in comparison to the porphyrin-stained *E. coli* cells with τ = 4.2 ns. A likewise observation for the fluorescence lifetime of porphyrins if they interact with bacteria cells already has been reported by *Russel et al.*. These changes are a result of a connection to intercellular components of the bacterial cell.[15]

3. Experimental

3.1 Analytic Methods

^{1}H-NMR and ^{13}C-NMR experiments were performed on a AVIII400, AVIIIHD500 and AVII600 from BRUKER. Chemical shifts are reported in ppm units with tetramethylsilane as an internal standard. ESI-MS measurements were performed on a FINNIGAN 8400-MSS I and MAT 4515. For the FLIM measurements a MicroTime 100 (MT100) setup from PICOQUANT (Berlin, Germany) was used. As the laser source a LDH-P-C375B for an excitation at 375 nm was used. A confocal microscope BX43 from OLYMPUS was equipped with a MPlanFLN objective with 100x magnification. The SymPhoTime 64 software was used for FLIM data acquisition and an image size of 465 x 465 pixels.

3.2 Bacteria Culture and Staining

For bacteria staining *E. coli* K12 was used. Lysogeny-Broth (LB) medium was used as growth medium. A colony from the cryoculture was added to 50 mL of liquid LB medium, then was grown at 37 °C on a shaker incubator (150 rpm) overnight followed by a subculture until an OD_{600} of 0.5 – 0.8 was reached. An amount of 20 mL bacterial suspension was harvested, washed three times with sterile phosphate-buffered saline (PBS, pH 7.2) and resuspended reaching an OD_{600} of 0.6 – 0.8. For the porphyrin staining a 20 mM stock solution of the porphyrin in DMSO has been diluted to 3 µM in PBS. The bacterial cells were then treated with this solution and incubated for 10 min at 37 °C in the dark on a shaker incubator (150 rpm). Afterwards the cells were washed with PBS by centrifugation and resuspension to remove the unbound porphyrin and were finally resuspended in PBS (OD_{600} of 0.8). The porphyrin-stained *E. coli* in PBS were then placed on a microscope slide and a coverslip was added before FLIM measurements.

3.3 Synthesis

All chemicals and solvents were purchased from ACROS ORGANICS (Fair Lawn, NJ, USA), SIGMA ALDRICH (St. Louis, MO, USA) and TOKYO CHEMICAL INDUSTRIES (Tokyo, Japan). The peptide was purchased from GENSCRIPT BIOTECH (Piscataway Township, NJ, USA). All syntheses were performed under nitrogen atmosphere in anhydrous solvents.

*S-(1-(4-(10,20-diphenylporphyrin)phenyl)-2,5-dioxopyrrolidin-3-yl)-L-cysteine (Porphyrin **7**)*

Porphyrin **6** (8 mg, 0.013 mmol) and *L*-cysteine (1.5 mg, 0.013 mmol) were dissolved in DMSO (2 mL) and the solution was stirred for 48 h at room temperature. The solvent was then given in Et_2O (100 mL), filtered and redissolved in CH_2Cl_2/MeOH (1/1, (*v*/*v*)). The solvent was evaporated and the product received as a red solid (6 mg, 61%). ^{1}H-NMR (500 MHz, DMSO-d^{6}): δ = –3.15 (br s, 2H), 1.25 – 3.50 (m), 7.85 – 7.87 (m, 8H), 8.25 – 8.26 (m, 6H), 8.86 – 8.91 (m, 4H), 8.97 (d, *J* = 4.5 Hz, 2H), 9.62 (d, *J* = 4.5 Hz, 2H) 10.56 (s, 1H) ppm. ESI-MS: Calcd. for $C_{45}H_{34}N_6O_4S$, 754.24 (100%); found ($M+H^+$), 755.24 (100%).

*S-(1-(4-(10,20-diphenylporphyrin)phenyl)-2,5-dioxopyrrolidin-3-yl)-N-amino-L-isoleucyl-L-phenylalanyl-L-cysteinyl-L-phenylalanyl-L-lysyl-L-arginyl-L-lysyl-L-arginyl-L-lysil-L-tryptophyl-L-leucyl-L-valyl-L-tyrosine (Porphyrin **8**)*

Porphyrin **7** (10 mg, 0.016 mmol) and the peptide YVLWKRKRKFCFI-Amide (27 mg, 0.016 mmol) were dissolved in DMSO (2 mL) and DIPEA (0.01 mL) in DMSO (0.1 mL) was added. The solution was stirred at room temperature for 48 h. The solvent was then given in Et_2O (100 mL), filtered and redissolved in CH_2Cl_2/MeOH (1/1, (*v*/*v*)). The solvent was evaporated and the product received as a red-brown solid (31 mg, 77%). ^{1}H-NMR (500 MHz, DMSO-d^{6}): δ = –3.16 (br s, 2H), 0.82 – 4.69 (m), 6.67 – 6.68 (m, 2H), 7.35 – 8.55 (m), 8.85 – 8.93 (m, 4H), 8.98 (d, *J* = 4.6 Hz, 2H), 9.42 (br s, 2H), 9.64 (d, *J* = 4.6 Hz, 2H) 10.59 (s, 1H), 10.80 (br s, 2H) ppm. ESI-MS: Calcd. for $C_{130}H_{162}N_{29}O_{16}S$, 2418.25 (100%); found ($M/2+H^+$), 1210.63608, ($M/3+H^+$), 807.42693, ($M/4+H^+$), 605.82254.

4. Conclusion

We successfully synthesized a porphyrin molecule which can be modified with a bioreceptor for bacteria linkage. Two possible bioreceptors, a cysteine and a peptide group, are used for the linkage of *E. coli* K12 cells. Within a staining process it was possible to show an interaction between the *E. coli* cell and the synthesized cysteine-porphyrin or peptide-porphyrin. An analysis with FLIM could already show a decrease of the fluorescence lifetime of the porphyrin molecule due to changes in their chemical environment or conformation as they have an interaction with cell components of the bacteria cells. These results show that both bioreceptors in combination with the porphyrin molecule can be used as a bio-linker on an electrode surface for further detection methods of bacteria.

Acknowledgements

The authors gratefully acknowledge the Lower Saxony Ministry for Science and Culture (MWK) for funding the Quantum- and Nanometrology (QUANOMET) project at the Laboratory for Emerging Nanometrology (LENA) and the Volkswagen Stiftung for funding the Project Laboratory Across Borders (ProLab).

References

1. A. Cassini, L. D. Högberg, D. Plachouras, A. Quattrocchi, A. Hoxha, G. Skov Simonsen, M. Colomb-Cotinat, M. E. Kretzschmar, B. Devleesschauwer, M. Cecchini, D. A. Ouakrim, T. C. Oliveira, M. J. Struelens, C. Suetens, D. L. Monnet, "Attributable deaths and disability-adjusted life-years caused by infections with antibiotic-resistant bacteria in the EU and the European Economic Area in 2015: a population-level modelling analysis", *Lancet Infect Dis*, vol. 19, pp. 56 – 66, 2019.
2. B. W. Brooks, J. Devenish, C. L. Lutze-Wallace, D. Milnes, R. H. Robertson, G. Berlie-Surujballi, "Evaluation of a monoclonal antibody-based enzyme-linked immunosorbent assay for detection of Campylobacter fetus in bovine preputial washing and vaginal mucus samples", *Veterinary Microbiology*, vol. 103, pp. 77 – 84, 2004.
3. J. Heo, S. Z. Hua, "An Overview of Recent Strategies in Pathogen Sensing", *Sensors*, vol. 9, pp. 4483 – 4502, 2009.
4. L. Zhu, J. He, X. Cao, K. Huang, Y. Luo, W. Xu, "Development of a double-antibody sandwich ELISA for rapid detection of Bacillus Cereus in food", *Sci. Rep*., vol. 6, pp. 16092 – 16102, 2016.
5. R. Paolesse, S. Nardis, D. Monti, M. Stefanelli, C. Di Natale, "Porphyrinoids for Chemical Sensor Applications", *Chem. Rev*., vol. 117, pp. 2517 – 2583, 2017.
6. L. Neumann, L. Könemund, V. Rohnacher, A. Pucci, H.-H. Johannes, W. Kowalsky, "A_2BC-Type Porphyrin SAM on Gold Surface for Bacteria Detection Applications: Synthesis and Surface Functionalization", *Materials*, vol. 14, pp. 1934 – 1948, 2021.
7. C. Brückner, J. J. Posakony, C. K. Johnson, R. W. Boyle, B. R. James, D. Dolphin, "Novel and improved synthesis of 5,15-diphenylporphyrin and its dipyrrolic precursors", *J. Porphyrins Phthalocyanines*, vol. 2, pp. 455 – 465, 1998.
8. X. Feng, M. O. Senge, "An efficient synthesis of highly functionalized asymmetric porphyrins with organolithium reagents", *J. Chem. Soc., Perkin Trans.*, vol. 1, pp. 1030 – 1038, 2001.
9. C. Liu, D.-M. Shen, Q.-Y. Chen, "Unexpected bromination ring-opening of tetraarylporphyrins", *Chem. Commun.*, pp. 770 – 772, 2006.
10. B. Shi, R. W. Boyle, "Synthesis of unsymmetrically substituted meso-phenylporphyrins by Suzuki cross coupling reactions", *J. Chem. Soc., Perkin Trans.*, vol. 1, pp. 1397 – 1400, 2002.
11. M. Sortino, V. C. Filho, R. Corrêa, S. Zacchino, "N-Phenyl and N-phenylalkyl-maleimides acting against Candida spp.: Time-to-kill, stability, interaction with maleamic acids", *Bioorg. Med. Chem.*, vol. 16, pp. 560 – 568, 2008.
12. P. Morales, L. Moreno, J. Fernández-Ruiz, N. Jagerovic, "Synthesis of a novel CB2 cannabinoid-porphyrin conjugate based on an antitumor chromenopyrazoledione", *J. Porphyrins Phthalocyanines*, vol. 21, pp. 67 – 76, 2017.
13. F. Liu, A. S. Y. Ni, Y. Lim, H. Mohanram, S. Bhattacharjya, B. Xing, "Lipopolysaccharide neutralizing peptide-porphyrin conjugates for effective photoinactivation and intracellular imaging of Gram-negative bacteria strains", *Bioconjugate Chem.*, vol. 23, pp. 1639 – 1647, 2012.
14. Y. Chen, T. Parr, A. E. Holmes, K. Nakanishi, "Porphyrinmaleimides : towards thiol probes for cysteine residues in proteins", *Bioconjugate Chem.*, vol. 19, pp. 5 – 9, 2008.
15. J. A. Russel, K. R. Diamond, T. J. Collins, H. F. Tiedje, J. E. Hayward, T. J. Farrel, M. S. Patterson, Q. Fang, "Characterization of Fluoreszence Lifetime of Photofrin and Delta-Aminolevulinic Acid Induced

Protoporphyrin IX in Living Cells Using Single- and Two-Photon Excitation", *IEEE Journal of selected Topics in Quantum Electronics*, vol. 14, pp. 158 – 166, 2008.

Proceedings of the SurfCoat Korea 2021 / Graphene Korea 2021 Joint Virtual International Conferences
May 26 – 28, 2021, (Held Virtually)
DOI: https://doi.org/10.26799/cp-surfcoat-graphene-korea-2021

Structure and phase formation of ion-plasma vacuum-arc Zr-B-Si-C-Ti-(N) coatings during deposition

Dmitry S. Belov, Igor V. Blinkov, Victor S. Sergevnin, Alexey V. Chernogor, Aleksandr P. Demirov, Boris Yu. Kuznetsov

Functional Nanosystems and High-Temperature Materials Department, National University of Science and Technology MISiS**,** 119049, 4 Leninsky prospect, Moscow, Russia, dm.blv@yandex.ru

Abstract

Zr-B-Si-C-Ti-N and Zr-B-Si-C-Ti coating systems were produced by arc-PVD technique. For their deposition, a combined titanium cathode with a ZrB2-SiC insert was used. Deposition was carried out in a residual atmosphere of N_2 and Ar. Coatings structure and composition were investigated. The Zr-B-Si-C-Ti coating is characterized by an amorphous-nanocrystalline structure. In this case, nanocrystallites were formed from complex (Zr, Ti) C, and the amorphous structure fraction is formed mainly by phases based on zirconium and silicon. The second system, deposited in a nitrogen residual atmosphere, Zr-B-Si-C-Ti-N, has a predominantly amorphous structure. Such a structure is formed mainly from borides, nitrides, carbides and complex compounds of zirconium, silicon and titanium.

Keywords: amorphous structure, nanocrystalline structure, complex carbide, arc-PVD, phase formation, functional coatings, bonds energy

1. Introduction

One of the most effective methods for protecting the surfaces of critical parts and assemblies exposed to high-temperature effects and loads is the application of various kinds of multifunctional coatings. A promising material for them is the ZrB_2-SiC composite, on the basis of which coatings are formed by plasma spraying to protect against high-temperature oxidation. However, the high porosity of such coatings, low cohesive and adhesive strength with the substrate do not make it possible to consider them as simultaneously increasing the wear-resistant characteristics of frictional structural elements. This work is devoted to studying the possibilities of forming coatings of this system by the arc-PVD method, which is widely used to create coatings for this purpose.

2. Results and Discussion

This work is devoted to studying the possibilities of forming Zr-B-Si-C-Ti-(N) coatings by the arc-PVD method using an combined evaporated cathode including a cylindrical powder composite insert of ZrB_2 (80 vol.% or 88.4 wt.%) - SiC (20 vol.% or 11.6 wt.%) with a diameter of 58 mm and a height of 15 mm, prepared by the method of spark plasma sintering, which was pressed into a titanium metal base with a diameter of 62 mm. The current and voltage of the evaporating arc were 110 A and 20 V, respectively. A negative bias potential of 120V was applied to the substrate. The partial pressure of nitrogen during the formation of Zr-B-Si-C-Ti-N coatings was 0.8 Pa. The argon pressure during the deposition of the Zr-B-Si-C-Ti coatings was maintained at 0.4 Pa. The coatings were deposited on substrates made of WC-Co alloy and heat-resistant nickel alloy. The deposition time was 60 minutes.

Proceedings of the SurfCoat Korea 2021 / Graphene Korea 2021 Joint Virtual International Conferences
May 26 – 28, 2021, (Held Virtually)
DOI: https://doi.org/10.26799/cp-surfcoat-graphene-korea-2021

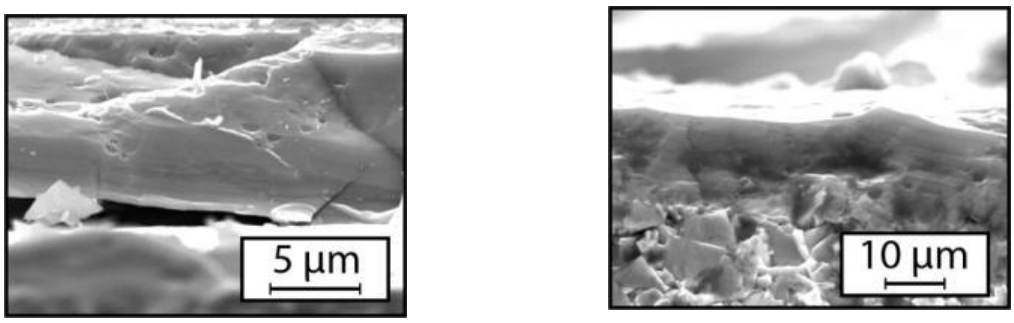

a) b)

Fig. 1: Images of transverse fractures of Zr-B-Si-C-Ti-N (a) and Zr-B-Si-C-Ti (b) coatings.

Figure 1 shows the results of fractographic studies of the coatings. For the Zr-B-Si-C-Ti-N coating, the failure occurs by a brittle cleavage mechanism with a characteristic feature of the formation of intergranular facets in the microrelief. The failure of the Zr-B-Si-C-Ti coating is ductile. It is accompanied by the formation of pits of a fibrous-banded fracture in the microrelief. The elemental composition of the formed coatings is shown in Table 1.

Table 1: Elemental composition of the obtained coatings*.

Residual atmosphere	Element content, at. %						
	N	C	B	Si	Zr	O	Ti
N_2	39.0	9.5	12.1	13.9	6.9	3.7	14.9
Ar	-	23.1	31.6	28.6	13.2	2.2	1.3

* The average composition of the evaporated cathode, taking into account the entire volume of its material that has passed into the vapor phase, at.%: C - 5; B - 30; Si - 5; Zr -15; Ti - 45

The diffraction patterns of the obtained Zr-B-Si-C-Ti-N and Zr-B-Si-C-Ti coatings are shown in Figure 2. Taking into account the presence of a halo at low diffraction angles, it follows from them that the composition of the coatings mainly contains X-ray amorphous phases. An approximate estimate indicates the degree of amorphization of the coating structure at the level of 88 % and 75 %, respectively, for the first and second coating compositions.

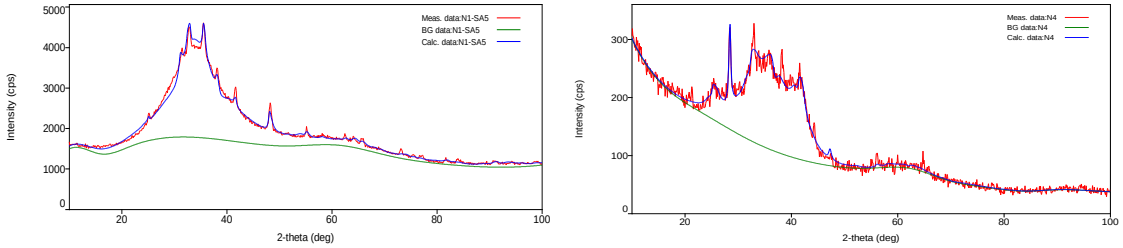

a) b)

Fig. 2: Diffractions patterns of of Zr-B-Si-C-Ti-N (a) and Zr-B-Si-C-Ti (b) coating samples

The study of the structure of the coatings by TEM and the obtained electron diffraction patterns (Figure 3) confirm the results of X-ray diffraction analysis on the predominantly amorphous structure of the coatings of both compositions and the greater degree of amorphization of the Zr-B-Si-C-Ti-N coatings. This is evidenced by the diffuse nature of the diffraction lines of electrons of this coating (Figure 3a), obtained from different parts of it, and high-resolution TEM images (Figure 3b). Electron diffraction patterns of the Zr-B-Si-C-Ti coating obtained from areas characterized by a darker contrast, in comparison with diffraction patterns from light areas, have a pronounced character and can be attributed to titanium carbide and boride (Figure 3c). In high-resolution images for this coating composition, crystallites up to ~ 10 nm in size were found in these regions (Figure 3d).

DOI: https://doi.org/10.26799/cp-surfcoat-graphene-korea-2021

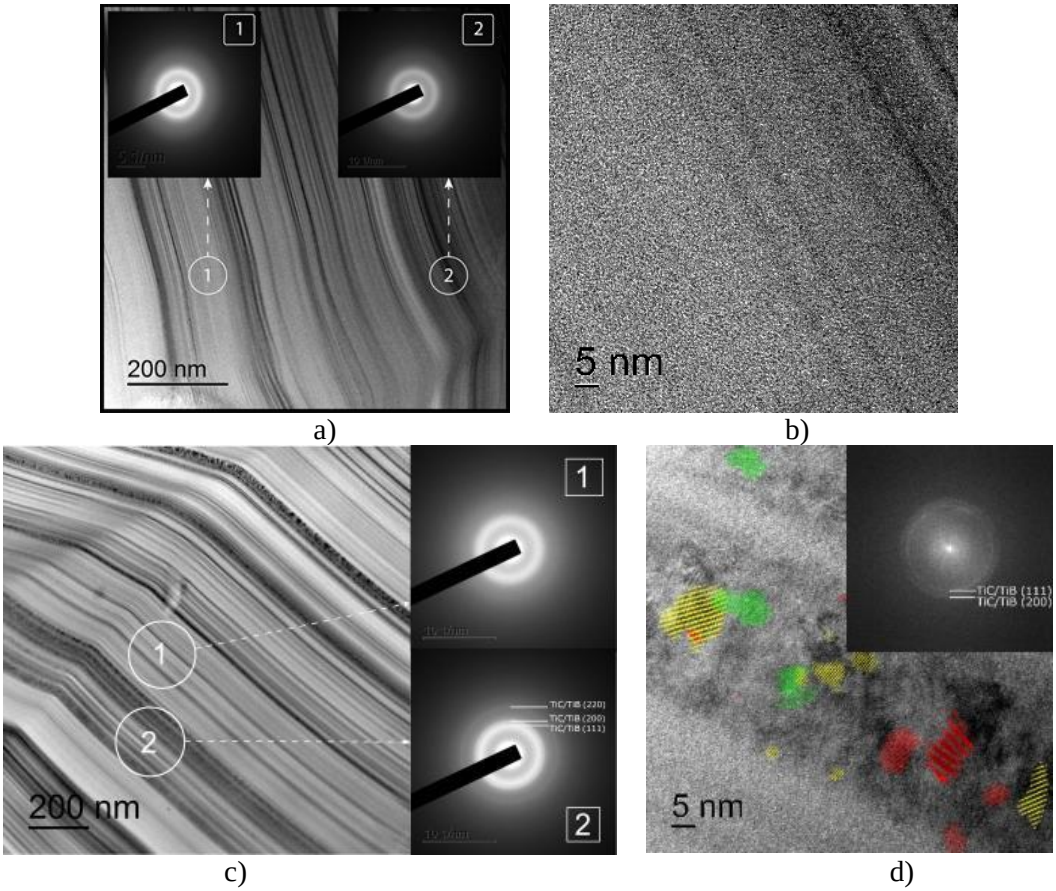

Fig.3: TEM images and electron diffraction patterns from different areas of the Zr-B-Si-C-Ti-N (a, b) and Zr-B-Si-C-Ti (c, d) coatings

In the images of cross-sections obtained in the bright-field mode, as noted above, areas with different contrast are observed (Figure 3, 4).

a)

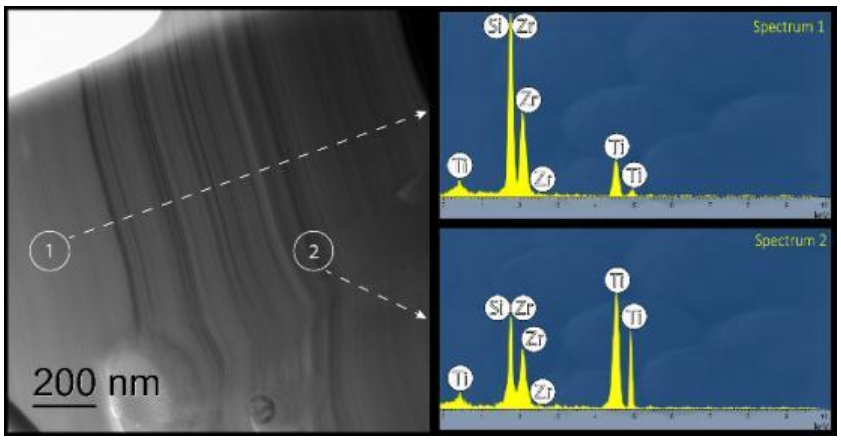

DOI: https://doi.org/10.26799/cp-surfcoat-graphene-korea-2021

b)

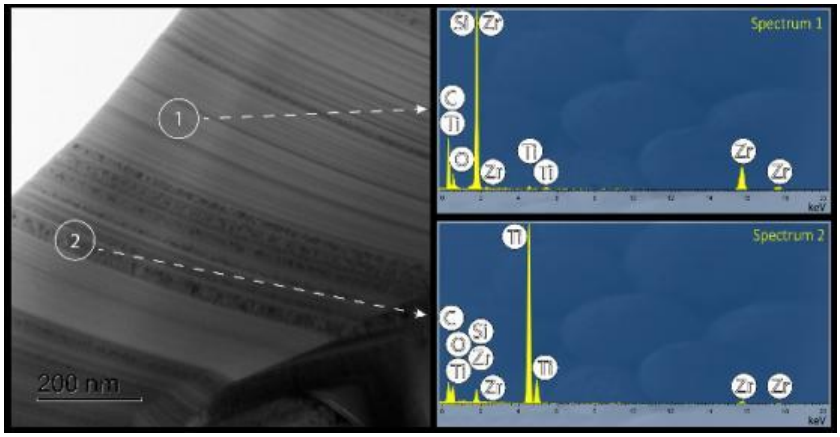

Fig. 4: Images of cross-sections of Zr-B-Si-C-Ti-N (a) and Zr-B-Si-C-Ti (b) coatings and characteristic EDX patterns from their various sections

On a sample of amorphous material of uniform thickness, this may indicate a mass contrast: in a region with a larger mass, electrons are scattered at large angles, and therefore the intensity (or brightness) of these regions in the obtained images is lower. The sizes of the regions of structural inhomogeneity of the coatings vary from 1 to 10 nm and from 1 to 50 nm for the Zr-B-Si-C-Ti-N and Zr-B-Si-C-Ti coatings, respectively; their periodicity is not observed. EDX analysis (Figure. 4 a, b) showed that Si and Zr prevail in the composition of phases in the light areas (area 1), and Ti prevail in the dark areas (area 2). Moreover, high-resolution images show that it is the dark regions in the structure of Zr-B-Si-C-Ti coatings that are characterized by a crystalline structure with a crystallite size of ~ 10 nm located in an amorphous matrix (Figure 3d). Taking into account, the obtained electron diffraction patterns, as noted above, these phases have fcc structures.

The XPS study of the Zr-B-Si-C-Ti-N coating indicates that Zr3d spectral line has three peaks. The main peak corresponds to 180.0 eV, which corresponds to zirconium carbide. The second peak at 180.6 eV is close to the reference value for ZrN (181.0 eV). The third peak with an energy of 183.2 eV is possibly associated with the presence of Zr – N and Zr – B bonds. The Si2p spectrum contains a peak with an energy of ~ 101.1 eV. This value is in the range of reference values for SiC (100.2 eV) and Si_3N_4 (101.8 eV) and, apparently, corresponds to silicon carbonitride. The Ti2p spectrum consists of one doublet (Ti2p2/3) - 454.7 eV, which is slightly lower than for titanium nitride (454.9 eV). Perhaps this is determined by the formation of Ti-Ti, Ti-C and Ti-B bonds. The B1s spectrum of boron is located at the energy value of 188.2 eV, which characterizes the energy of Zr-B bonds. In the Zr-B-Si-C-Ti coating for the Ti2p2/3 spectrum, a peak of 454.8 eV is observed, which can be interpreted as titanium with a mixed type of Ti-Ti and Ti-C bond. The spectrum of Zr3d contains a peak at 179.7 eV. Its comparison with E_b for Zr, ZrB_2 and ZrC - 178.9; 178.9; 180.0 eV suggests that it is closer to ZrC with the addition of Zr-B or Zr-Zr bonds. The B1s spectrum of boron, as for the first composition of the coating, is located at E_b 188.2 eV, which suggests the presence of Zr–B bonds. Two peaks are observed in the Si2p spectrum: 99.9 and 101.1 eV. The main peak at 99.9 eV can be attributed to silicon carbide with a small fraction of Si – Si bonds. The second peak exceeds the SiC reference value (100.2 eV), so it can be attributed to SixOyCz, which is consistent with the presence of oxygen in the coating.

3. Conclusion

Coatings were obtained in the Zr-B-Si-C-Ti-N and Zr-B-Si-C-Ti systems by vacuum arc evaporation of ZrB_2-SiC-Ti combined targets in a residual atmosphere of N_2 and Ar. The Zr-B-Si-C-Ti-N coating has a predominantly amorphous structure, formed mainly on the basis of nitride, carbide, boride phases and complex compounds of Zr, Si, Ti. The Zr-B-Si-C-Ti coating is characterized by an amorphous-nanocrystalline structure. The amorphous component of this coating is formed mainly by phases based on Zr and Si. The nanocrystalline structure is based on titanium carbide. The increased degree of amorphization of the structure of the Zr-B-Si-C-Ti-N coatings can be associated with a higher cooling

DOI: https://doi.org/10.26799/cp-surfcoat-graphene-korea-2021

rate of the forming coating due to the higher thermal conductivity of the residual nitrogen atmosphere as compared to argon.

Proceedings of the SurfCoat Korea 2021 / Graphene Korea 2021 Joint Virtual International Conferences
May 26 – 28, 2021, (Held Virtually)
DOI: https://doi.org/10.26799/cp-surfcoat-graphene-korea-2021

The effect of the addition of granite powder to the primer on the pull-off strength of epoxy resin coatings

Ł. Kampa[1]
[1] Wroclaw University of Science and Technology, Wybrzeże Wyspiańskiego 27, 50-370 Wroclaw, Poland

Abstract

This article describes the effect of adding waste granite powder to the epoxy resin layer on its pull-off strength. The substrate was C30 / 37 concrete. The priming resin was modified with 10%, 20%, 30%, 40%, 50%, and 60% of granite powder. For control purposes, a sample was also made without the addition of powder. For each material configuration, four strength tests were carried out with the use of an automatic device recording both the pull-off strength and the measurement time. The obtained results were compared with the control sample. The best result in the test was obtained with the addition of 20%, which gave an increase of 19% compared to the reference sample. An equally good result was obtained with the addition of 10% granite powder (increase by 11%). The addition of a larger amount of the additive resulted in a decrease or a slight increase in the pull-off strength compared to the reference sample. Additionally, the additive has been found to darken the coating, and the coating becomes completely opaque when added above 50%.

Keywords: resin floors, pull-off strength, granite flour, industrial waste

1. Introduction

Epoxy resins are a popular method of finishing large warehouse areas, both due to their chemical resistance and good strength parameters. On the other hand, granite powder, which is actually waste from the mining industry, has little use, or rather it is an attempt at its disposal. It is used as ballast for concrete or paving stones, or even as fertilizer. Granite powder does not contain any compounds hazardous to humans or animals, but due to its lightness, it can be dispersed, contaminating the vicinity of the heap, because the most popular methods of its storage are open landfills.

All kinds of rock powders are quite a popular way to modify the properties of cement composites. The study [1] presents the effect of adding marble powder,, granite powder and mixed powder to SCC self-compacting concrete. Granite powder turned out to be better, but both resulted in improved mechanical properties of the product, including tensile and flexural strength. Li et al. [2] added granite dust to reduce the amount of added cement and at the same time increase the strength of the mortar. They point out that this method allows for the removal of waste (granite dust) and the carbon footprint. This technology, as the authors point out, is better than a method of replacing cement to utilize waste and reduce cement content. It also improves the strength and microstructure of the tested mortar. In turn, the addition of fly ash improves the mechanical parameters [3]. The use of 20% silica ash causes beneficial changes in the microstructure and improves the mechanical parameters (including crack resistance) of mature concrete. In addition, the use of fly ash or granite powder allows to reduce the cost of cement flooring, while improving the mechanical properties [4]. Belebchouche et al. [5] showed that the addition of crushed glass in the amount of 15% improves the mechanical strength, obtains a higher degree of hydration, and reduces porosity

There are also many studies describing the influence of various types of resin coating additives. The addition of nanosilica and multiwall carbon nanotubes to resin coatings improves the bond between polymer composites [6]. Pourhashema et al. [7] proved that the addition of a hybrid SiO2-graphene oxide to the resin improves the anti-corrosive properties of such a coating, its adhesion, and properties when in contact with water. A simple way to improve the adhesion of the epoxy coating, without mechanically treating the substrate, is to add glass powder [8], appropriate polymers [9], or monomers [10]. Atta et al. [11] proved that graphene oxide added to the resin provides lower water absorption. A simple way to improve the pull-off strength of the coating is to use polypropylene fibers for the epoxy primer layer [12]. An appropriate modification of the substrate is an equally effective and popular way to improve the final properties of the coating. Chowaniec et al. [13] investigated the effect of adding glass powder to the resin. The addition of 40% increased the pull-off strength. Surface texturing allows to increase the pull-off strength of coatings [14]. The most advantageous method turned out to be the imprinting of crosses in the shape of "+", which required appropriate care and precision in forming shapes, depth, spacing, etc. On the other

DOI: https://doi.org/10.26799/cp-surfcoat-graphene-korea-2021

hand, Sadowski et al. [15] drew attention to the proper use of epoxy coatings, which are often used in warehouse facilities. They found that the main cause of the failure was the spinning of the trolley's drive wheels, which in turn led to a local temperature rise and thermal shock to which the floor was not resistant. This shows how important it is to use this type of coating properly.

The main aim of the research was the lack of unequivocal research on the direct addition of granite powder to epoxy coatings. Therefore, it was decided to test the effect of adding 10%, 20%, 30%, 40%, 50%, and 60% granite powder to the epoxy primer layer on the concrete substrate of C30 / 37 concrete. For control purposes, a sample was made without the addition of powder, which was later compared with the tested coatings.

2. Materials, methods, and results

2.1. Concrete substrate

The substrate on which the test was performed was C30 / 37 concrete with a slow development of strength, which was ordered from a specialized company producing concrete mix. The degree of watertightness is W8, consistency class S3, and a maximum grain size of 16mm. The air content was 2.5% ± 1%. Concrete was stored for 28 days at 20 ° C.

2.2. Granite powder

The granite powder used in the epoxy coating was wasted from the extraction of granite aggregate. To control the grain thickness, an analysis was carried out on the control sieves. Fraction up to 0.02mm accounted for 5%, 0.02-0.032mm was the largest percentage - 46.9%. 31% was the fraction 0.032-0.063mm, 7.3% the fraction 0.063-0.1mm, 8.7% the fraction 0.1-0.14mm, and above 0.14mm - 1.1%.

2.3. Epoxy Resin

The epoxy resin Meteor Primer (Si-Tech Sp. Z O.O., Dobra 9, 05-306, Jakubów) was the modified base layer in this study. It was characterized by a density of 1–1.2 g / cm3, a viscosity of 400–600 MPa · s, working life (at 20 ° C) 20–30 minutes and full hardening after 24 hours. The resin is the result of the reaction of bisphenol A with epichlorohydrin (epoxy resin - average molecular weight ≤ 700).

2.4. Pull-off strength

The made substrate was sanded with fine sandpaper. After that, the surface was degreased with acetone. The individual research fields were separated with a bituminous roofing sealant. Each area was 20 x 20 cm. Then the resin was prepared. The resin consisted of two components: A and B in the ratio 100: 33. In this study, it was decided to test the addition of 10%, 20%, 30%, 40%, 50%, and 60% by weight. granite powder. The appropriate amount of component A was poured into a tared plastic cup placed on a balance. Granite powder was then added while weighing it. After these two elements were mixed, the appropriate amount of component B was added. For control purposes, a sample was also made without the addition of powder. The mixture was poured on individual research fields, creating a coating with a thickness of about 3 mm. It was vented with a brush with hard bristles. After it had hardened, holes with a diameter of 50 mm and a depth of 5 mm were made to test the pull-off strength. The steel discs were glued to the coating with the epoxy resin Epidian 5 with the Z1 hardener from Ciech Sarzyna (proportion 100: 12). Figure 1a shows the cross-section of the coating and the disc connecting it to the pull-off strength tester.

In 11 out of 28 tests, coating-substrate detachment was found. This was mainly the case with more granite powder. This may indicate that the resin, while still in the liquid state, was so dense that it was not able to reach every pore on the surface of the substrate. As a result, the proper fusion of these two surfaces did not occur.

Figure 1b shows a diagram of the dependence of the pull-off strength of the epoxy resin coating on the concrete substrate depending on the amount of granite powder added. It shows that the best result in the test was 3.40 MPa, with the addition of 20% granite powder. This resulted in an increase in strength compared to the reference sample (2.88MPa) by 0.52MPa, i.e., 18%. This shows that the strength can be improved with little effort. The second result in the test was obtained with the addition of 10% granite powder. The pull-off strength was 3.20 MPa - strength increase by 11% (0.32 MPa). When 30% of the powder was added, the test result was the lowest - 2.49MPa. With the addition of 40%, you can also see an increase in strength compared to the reference sample (increase by 0.06MPa). A greater amount of granite powder resulted in a decrease in strength compared to the reference sample.

DOI: https://doi.org/10.26799/cp-surfcoat-graphene-korea-2021

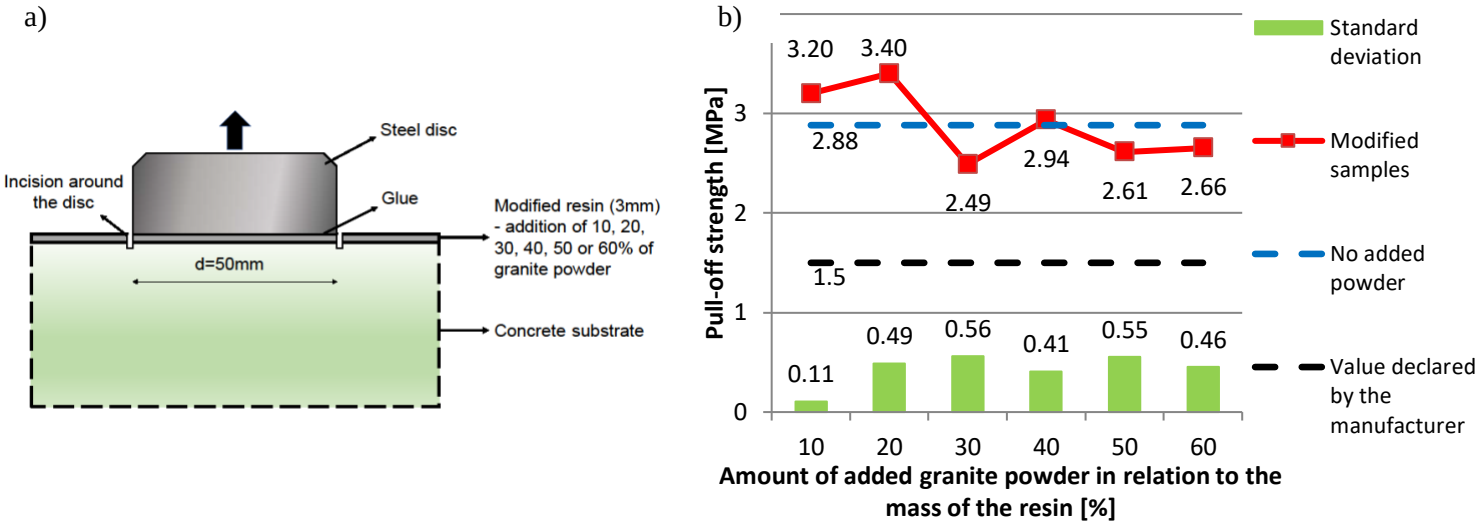

Figure 1. Test samples: a) Cross-section through the tested coating and the disc connecting it with the strength testing device, b) Dependence of the pull-off strength of the epoxy resin coating on the substrate depending on the amount of granite powder added.

3. Cost-economic analysis

In view of the ever-increasing prices, savings are increasingly being sought in all industries, especially in construction, therefore a cost-economic analysis was carried out to verify the main costs associated with the coating. The focus was only on the direct purchase cost of epoxy resin and granite powder. The price of resin was assumed as 200 € / 12.5 kg, and for granite powder 8,90 €/1000 kg. The summary of costs for individual samples subjected to the endurance test is presented below in Table 1.

Table 1. A summary of the costs of making the tested coating depending on the amount of granite powder added

Addition [%]	Resin content [%]	Granite powder content [%]	Epoxy resin cost [€/m2]	Granite powder cost [€/m2]	Total cost [€/m2]	Pull-off strength [MPa]
0	100	0	6,7	0,00	6,70	2,88
10	90	10	6	0,01	6,01	3,20
20	80	20	5,3	0,01	5,31	3,40
30	70	30	4,6	0,02	4,62	2,49
40	60	40	4	0,02	4,02	2,94
50	50	50	3,3	0,03	3,33	2,61
60	40	60	2,7	0,03	2,73	2,66

The table clearly shows that the price per square meter decreases with the increasing amount of granite powder. In the most favorable case, due to the pull-off strength of the coating (20% of the powder), it gives a final cost saving of 1.39€ / m2, which means a cost reduction of 20%. This simple calculation clearly shows that it is easy to reduce the cost of making the coating and increase its pull-off strength.

4. Conclusion

Waste rock powders are the subject of various types of articles. However, the topic of connecting granite powder with epoxy resin is not anymore. This article examines the mechanical properties and performs an economic analysis of the modified coatings. The main aim of this study was to obtain the highest possible pull-off strength

DOI: https://doi.org/10.26799/cp-surfcoat-graphene-korea-2021

of the coating and to reduce costs as much as possible. Therefore, the test was carried out on a concrete substrate, where the influence of the addition of 10%, 20%, 30%, 40%, 50%, and 60% of granite powder to the epoxy resin primer was analyzed. The obtained results were compared with the reference sample (without the addition of powder). The main conclusions of the study are:
- It has been found that the optimal content of granite powder is 10-20 wt.%. This value increases the strength of the coating, which increases the strength of the coating by up to 18% compared to the reference sample. A larger amount of powder caused a reduction or a very slight increase in strength,
- Economic analysis has shown that adding even a small amount of granite powder to the coating results in a significant reduction in coating costs. If 20% of the powder is added, it reduces the costs by 20%.

Funding

The author received funding from the project supported by the National Centre for Research and Development, Poland [grant no. LIDER/35/0130/L-11/19/NCBR/2020 "The use of granite powder waste for the production of selected construction products."

References

1. Sadeka, D.M, El-Attarb, M.M, Alib, H.A., Reusing of Marble and Granite Powders in Self-Compacting Concrete for Sustainable Development, Journal of Cleaner Production (2016),
2. Li, L.; Wang, Y.; Tan, Y.; Kwan, A. Filler technology of adding granite dust to reduce cement content and increase strength of mortar. Powder Technol. 2019, 342, 388–396,
3. Golewski, G.L. The influence of microcrack width on the mechanical parameters in concrete with the addition of fly ash: Consideration of technological and ecological benefits. Constr. Build. Mater. 2019, 197, 849–861,
4. Chajec, A. (2021). Granite Powder vs. Fly Ash for the Sustainable Production of Air-Cured Cementitious Mortars. Materials, 14(5), 1208,
5. Belebchouche, C., Moussaceb, K., Bensebti, S. E., Aït-Mokhtar, A., Hammoudi, A., & Czarnecki, S. (2021). Mechanical and Microstructural Properties of Ordinary Concrete with High Additions of Crushed Glass. Materials, 14(8), 1872,
6. Morshed, S.A.; Young, T.J.; Chirdon, W.M.; Zhang, Q.; Tatar, J. Durability of wet lay-up FRP bonded to concrete with Nanomodified Epoxy Adhesives. J. Adhes. 2020, 96, 1–26,
7. Pourhashema, S.; Vaezia, M.; Rashidib, A. Investigating the effect of SiO2-graphene oxide hybrid as inorganic nanofiller on corrosion protection properties of epoxy coatings. Surf. Coat. Technol. 2017, 311, 282–294,
8. Chowaniec, A.; Sadowski, Ł.; Żak, A. The chemical and microstructural analysis of the adhesive properties of epoxy resin coatings modified using waste glass powder. Appl. Surf. Sci. 2020, 504, 144373,
9. Do, J.; Soh, Y. Performance of polymer-modified self-leveling mortars with high polymer–cement ratio for floor finishing. Cem. Concr. Res. 2003, 33, 1497–1505,
10. Ahn, N. Effects of diacrylate monomers on the bond strength of polymer concrete to wet substrates. J. Appl. Polym. Sci. 2003, 90, 991–1000,
11. Chowaniec, A., & Ostrowski, K. (2018). Epoxy resin coatings modified with waste glass powder for sustainable construction. Czasopismo Techniczne, 2018(Volume 8), 99-109,
12. Atta, A.M.; Al-Hodan, H.A.; Hameed, R.S.A.; Ezzat, A.O. Preparation of green cardanol-based epoxy and hardener as primer coatings for petroleum and gas steel in marine environment. Prog. Org. Coat. 2017, 111, 283–293,
13. Kampa, Ł.; Chowaniec, A.; Królicka, A.; Sadowski, Ł. The Effect of the Addition of Polypropylene Fibers to Primer on the Pull-Off Strength of Epoxy Resin Coatings, Materials 2020, 4674,
14. Krzywiński, K.; Sadowski, Ł. The effect of texturing of the surface of concrete substrate on the pull-off strength of epoxy resin coating. Coatings 2019, 9, 143,
15. Sadowski, Ł., Hoła, J., Żak, A., & Chowaniec, A. (2020). Microstructural and mechanical assessment of the causes of failure of floors made of polyurethane-cement composites. Composite Structures, 238, 112002.

Proceedings of the SurfCoat Korea 2021 / Graphene Korea 2021 Joint Virtual International Conferences
May 26 – 28, 2021, (Held Virtually)
DOI: https://doi.org/10.26799/cp-surfcoat-graphene-korea-2021

Finite element simulation of residual stresses and failure mechanism of plasma sprayed thermal barrier coatings considering real interface

Ahmed Abdelgawad, Khaled Al-Athel

[1]King Fahd University of Petroleum and Minerals, Dhahran, Saudi Arabia, g201705510@kfupm.edu.sa
[2]King Fahd University of Petroleum and Minerals, Dhahran, Saudi Arabia, kathel@ kfupm.edu.sa

Abstract

In order to increase the efficiency of gas turbine engines, which are used for propulsion and electricity generation, the turbine inlet temperature (TIT) has to be as high as possible. Using Thermal Barrier Coatings (TBC) allows the metallic internal components to operate at elevated temperature near to its melting temperature. Thermally growing oxide induces cracks formation in the top coat that may lead to complete failure TBC due to spallation. This research aims at investigating the development of the stresses and critical cites that have possibility of crack nucleation due to thermal mismatch during operating cycle of a typical plasma sprayed TBC. A true finite element model was developed based on a scanning electron microscope image taking the advantage of a commercial finite element package (ABAQUS) and image processing techniques. The model including the effect of creep on all layers and plastic deformation of BC, TGO and substrate. The results show that unlike common unit cell models in literature, a better understanding can be achieved by having a model based in an SEM image that represents the real geometry.

Keywords: Micromechanics, Thermal barrier coatings, Residual stresses, Finite element modelling (FEM).

1. Introduction

Thermal barrier coating (TBC) is an arrangement of advanced materials that are usually applied to metallic surfaces that operates at very high temperatures, such as a gas turbine or aero-engine. The main function of TBC is to produce a temperature difference through the TBC layers so that the life of the component can be enhanced by reducing oxidation and thermal fatigue. These coatings isolate the blade/vine surfaces from the flow of hot and corrosive gases by using of materials that have a very low thermal conductivity, which can result in a considerable temperature drop between the coating surface and the load-bearing material. In combination with active film cooling, TBCs can permit operating temperatures as high as the melting temperature of the base metal without causing any structural or corrosive damage, thereby resulting in a higher thermal efficiency of a thermodynamic system [1].

TBC systems have been studied extensively to understand different failure mechanisms that can lead to spallation or delamination of TC. Many numerical and experimental studies have been carried out to investigate the factors that may lead to failure of TBC such as creep, oxidation, phase transformation, etc. In experimental studies, it very difficult to track the crack propagation in real time, and numerical studies mostly deal only with 2D models that cannot track the crack propagation. Most 2D models consider the interface between TC and TGO/BC to be sinusoidal and neglect the porosities. However, with advances in image processing, scanning electron microscope (SEM) images can be converted into CAD models and then used in any finite element package. Chen Lin et al. [2] used a threshold values to assign image pixels to specific materials depending on their grey scale generated by SEM, and then converted these pixels into mechanical mesh considering pixels position coordinates as nodes coordinates that will be used to reconstruct finite element mesh. M.O.A program developed by M. Rangbar et al. [3] was used to represent the porosities within lamellar ceramic layer. The interface between the layers can be defined in terms of Fourier series and then use this equation to shift the meshing to fit the two lines defined by Fourier series. This method can work only for defining the interface line between the two phases but not for defining the internal porosities and cracks [4]. Object oriented finite element (OOF2) - a tool that has been developed by National Institute of Standards and Technology (NIST) in United States - is also able to generate mesh for the 2D images from SEM [5].

Previous techniques either use external codes to generate virtual topology and then use any FE package to generate mesh, or use image processing techniques to get an image that has different color for each layer, then use the developed code to generate FE mesh based on color. In this work, a new method is proposed to convert SEM

images of a TBC system into a very detailed CAD model that includes the interface as well as the pores, and can be imported into any FE software.

2. Modelling Procedure

2.1. Image Processing

Scanning Electron Microscope (SEM) was used in composition mode with backscatter electrons to have an image with different color tones associated with each material as shown in Fig 1-a. The image was captured at magnification of 500x with LYRA3 TESCAN. Image resolution was set to highest available option, 1024x1144 pixels, to get an image with good details that will be used in the following steps. Accelerating current was set to 30KV in order to achieve deepest points and get actual shape of pores. SEM image was imported into image processing software to increase the color contrast between the TC and BC layers, different filters were used. The type of filter has a significant effect on the quality of image as in Fig 1-b. To obtain the actual interface between the BC the TC, segmentation process was carried out based on the color difference obtained in the previous step. A perfect contact between the two layers was assumed and pores at the interface were neglected. After segmenting the image into two different partitions with different colors, the width of the selected geometry was set to 140 µm. Fig 2-a shows the segmented image.

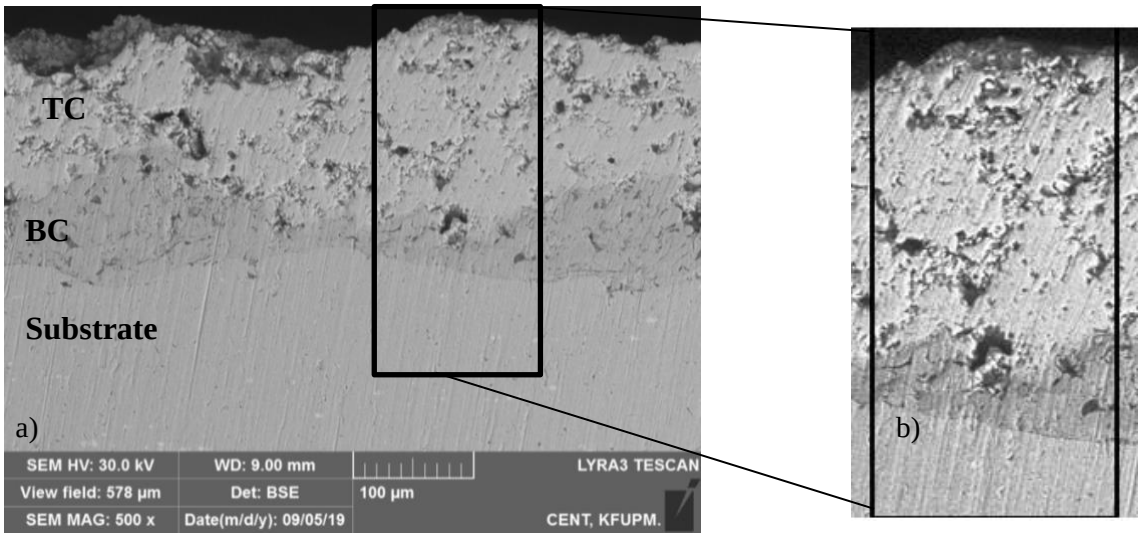

Fig 1 a) SEM image of TBC sample b) after applying filters

To obtain a solid surface that can be imported into any FE software, image tracing technique was used to convert a pixel-based image into a vector image consists of a set of splines as shown in Fig 2-b. After obtaining the solid surface as in Fig 2-c, the model is meshed as in Fig 2-d with 8-noded quadrilateral elements. Quadratic shape functions allow higher order displacement interpolation, and hence provide more accurate distribution of stress/strain fields with minimum size of 0.5 µm in order to capture the detailed interface between TC and BC. A TGO with thickness of 5 µm was introduced by shifting the interface between the TC and BC.

2.2. Simulation Conditions and Material Properties

A 140 µm wide TBC system is considered for this study, with temperature dependent material. Thermal loads and boundary conditions were defined to simulate a common thermal cycle of a TBC.

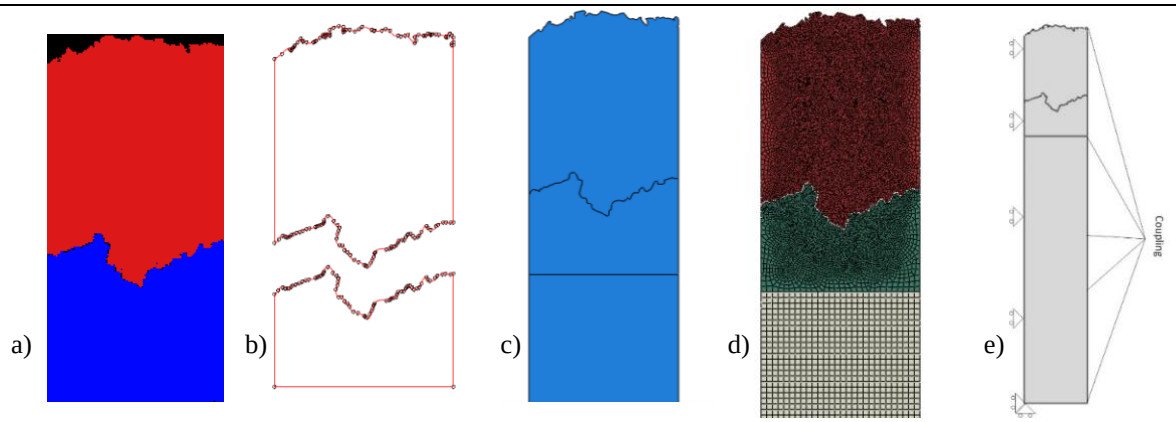

Fig 2 a) Image after segmentation, b) Interface definition, c) Generated Solid Surface, d) Generated mesh, e) mechanical boundary conditions

Fig 2-e shows the mechanical boundary conditions of the TBC FE model. The left edge is defined with roller support. All the nodes on the right edge are coupled horizontally. The node on the bottom left was completely fixed. To simulate thermal working conditions, three fully coupled thermos-mechanical steps were defined to present heating to 1200°C in 300 seconds, holding for two hours, and cooling to 25°C in 300 seconds of the TBC system considering non-homogeneous thermal loading. Generalized plane strain condition is widely used in simulation of thermal barrier coatings to allow deformation domain in the third direction (perpendicular to the page) to be finite in contrast to ordinary plane strain condition [5].

A TBC system usually consists of three layers. A TC, which is Yttria stabilized zirconia (YSZ) that is used to produce temperature difference to protect the substrate. A BC that is a metallic alloy (MCrAlY) used as a transition layer between the TC and the substrate to mediate the contact between the two layers, and to prevent oxidation of the substrate through formation of TGO. The third layer is the TGO layer that is formed at the surface of the BC due to the oxidation process. The substrate is Ni-based super alloy. BC, TGO and substrate are considered as elastic-perfectly-plastic materials with Von-Mises plasticity law used to describe plastic behavior. The TC is considered as an elastic material. Norton creep model used to describe the behaviour of all layers as giving by Eq (1)

$$\dot{\bar{\epsilon}}^{cr} = A\bar{\sigma}^{n} \tag{1}$$

where $\dot{\bar{\epsilon}}^{cr}$ is critical strain rate, A is Norton creep model pre-factor, $\bar{\sigma}$ is equivalent Von-Mises stress and finally n is Norton creep law exponent. Temperature dependent material properties are listed in Table 1 based on previous studies [3, 7, 8].

Table 1 temperature dependent material properties for all layers

	Substrate	**BC**	**TGO**	**TC**
Temperature range (T), °C	25-1100	25-1100	25-1100	25-1100
Young Modulus (E), GPa	184	200-110	400-320	48-22
Poisson's Ratio (ν)	0.3	0.3-0.33	0.23-0.25	0.1-0.12
Thermal Conductivity (K), W/m.k	26	4.3	25	26
Yield Strength (σ_y) MPa	1185-740	426-114	10000-1000	
Specific Heat (C), J/Kg.K	450	501	857	483
Thermal expansion (αx 10^{-6}) C^{-1}	12.6-16.3	13.6-17.6	8-9.6	9-12.2

3. Results and discussion

In case of as-sprayed conditions, stresses were found to be compressive at valleys and slopes while the peaks have tensile stresses that exceeds the strength of the TC (10-100 MPa). Since yielding is considered the threshold of crack formation [3], this leads to formation of micro-cracks at the peaks. This stress state changes after the growth of the TGO to be tensile at the valleys and slopes and compressive at the peaks, which exceeds the yield strength as in Fig 5. This conforms that cracks initiates at the peaks and when the stresses inverted, cracks continue towards

the valleys till complete failure occurs, which validates the stress inversion theory and results in growth of horizontal cracks between the valleys [7, 9, 10].

The regions in circle in Fig 5 has the highest compressive and tensile stresses in both cases with and without TGO, which also has the highest amplitude in the proposed interface. This leads to confirm that with increasing of the amplitude, the developed residual stresses also increase. The stresses in BC in both cases do not exceed 270 MPa - strength of BC- hence no micro-cracks are supposed to appear in BC due to thermal cycling or formation of the TGO.

4. Conclusion

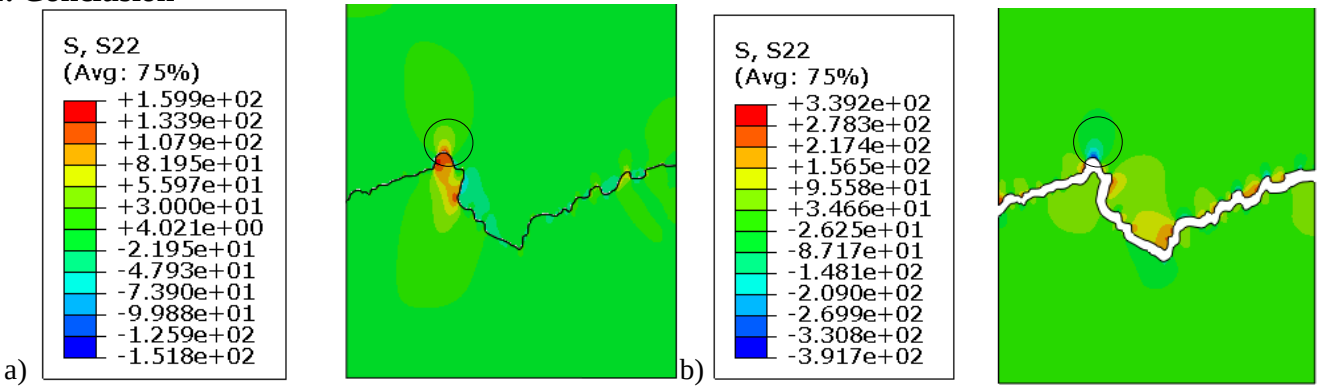

Fig 3 Stress after cooling cycle a) as-sprayed condition b) 5 µm

A new technique was developed to generate a solid geometry that represents the actual interface between the TC and BC from a typical SEM image, which can open the door for considering the effect of porosity in TBC systems or use this method for simulation of failure in many fields as composites for example. Also, generation of solid geometry that is usable in any commercial FE package make it is possible to obtain quadrilateral element mesh that allows using of XFEM code included in ABAQUS. Finally, FEM simulation resulted in excellent agreement of stress inversion theory. The developed model was used to have a clear description of the changes in the stress state during heating-dwelling-cooling stages, and hence, develop a better understanding of crack initiation.

References

[1] A. A. Abubakar, S. S. Akhtar, and A. F. M. Arif, "Phase Transformation Stress Field Due to Hot Corrosion in the Top Coat of TBC IMECE2013-63138 PHASE TRANSFORMATION STRESS FIELD DUE TO HOT CORROSION IN," no. May, 2014.

[2] D. Property and C. Behavior, "Oxidation Simulation of Thermal Barrier Coatings with Actual Microstructures Considering Strength Difference Property and Creep-Plastic Behavior," 2018.

[3] J. Absi and G. Mariaux, "Finite Element Modeling of the Different Failure Mechanisms of a Plasma Sprayed Thermal Barrier Coatings System," vol. 21, no. December, pp. 1234–1244, 2012.

[4] V. Maurel, E. P. Busso, J. Frachon, J. Besson, and F. N. Guyen, "International Journal of Solids and Structures A methodology to model the complex morphology of rough interfaces," *Int. J. Solids Struct.*, vol. 51, no. 19–20, pp. 3293–3302, 2014.

[5] M. Gupta *et al.*, "Influence of Topcoat-Bondcoat Interface Roughness on Stresses and Lifetime in Thermal Barrier Coatings," vol. 23, no. January, pp. 170–181, 2014.

[7] W. Zhu, Z. B. Zhang, L. Yang, Y. C. Zhou, and Y. G. Wei, "Spallation of thermal barrier coatings with real thermally grown oxide morphology under thermal stress," *Mater. Des.*, vol. 146, pp. 180–193, 2018.

[8] M. Mohammadi, E. Poursaeidi, and K. Torkashvand, "Surface & Coatings Technology Finite element analysis of the effect of thermal cycles and ageing on the interface delamination of plasma sprayed thermal barrier coatings," *Surf. Coat. Technol.*, vol. 375, no. June, pp. 243–255, 2019.

[9] S. Giesen, D. Sto, S. Giesen, D. Sto, and F. Ju, "Lifetime of Plasma-Sprayed Thermal Barrier Coatings : Comparison of Numerical and Experimental Results," vol. 18, no. December, pp. 835–845, 2009.

[10] M. Bäker, "Finite element simulation of interface cracks in thermal barrier coatings," vol. 64, pp. 79–83, 2012.

Proceedings of the SurfCoat Korea 2021 / Graphene Korea 2021 Joint Virtual International Conferences
May 26 – 28, 2021, (Held Virtually)
DOI: https://doi.org/10.26799/cp-surfcoat-graphene-korea-2021

Nacre Shell Inspired Self Assembly of Graphene Oxide-Lipid Nanocomposites

C R Greeshma[1], Dhyanesh Baskaran[1], Abhijit Mishra[1]

[1] Materials Science and Engineering, Indian Institute of Technology, Gandhinagar, Gujarat, India

Abstract

Nanoscale graphene oxide-lipid composites have shown wide applications in the field of biosensing and nanosafety. Macroscopic free-standing membranes of this combination potentially offer excellent mechanical properties which can be attributed to the inherent strength of graphene oxide(GO). Previous experimental studies have mostly dealt with monolayer or bilayer interactions of lipids with graphene and graphene oxide surfaces. In our study, we report for the first time, a simple and scalable fabrication method where Small Unilamellar Vesicles (SUVs) of 1,2-dioleoyl-sn-glycero-3-phosphocholine(DOPC) combine with graphene oxide to produce stable nanocomposites via self-assembly. Scanning Electron Microscopy (SEM) images of the composite revealed layer-by-layer structures, reconfirmed by X-Ray Diffraction(XRD) results which show a proportional increase in the interlayer separation with an increasing ratio of lipid in graphene oxide. The nanocomposite thus fabricated mimics naturally occurring nacre shell structures where graphene oxide substitutes the strong aragonite layers, and the intermediate lipid layers provide the necessary elasticity pertaining to protein chitin in nacre. The addition of lipids to graphene-based nanocomposites also serves as a biodegradable alternative to using polymers as a popular reinforcement agent. The ease of fabrication method reported facilitates the production of stable GO-Lipid membranes in variable scales and geometries.
Keywords: self-assembly, graphene oxide, bionanocomposite, lipids, nacre shell, biomimetics, free-standing membrane

1. Introduction

Nacre shell structures are known for their exceptional mechanical properties and their associated applications[1]. Aragonite, a form of $CaCO_3$, and beta chitin, a form of protein are found to arrange in alternate layers in natural nacre. This brick and mortar arrangement contributes to the combined strength and toughness in the nacre that surpasses individual constituent properties. In the past, there have been various attempts to mimic these structural features to fabricate mechanically strong composites. Graphene, the strongest material on earth were used in place of the hexagonal aragonite sheets in many studies. A majority of the past fabricated composites, however, used polymers as the intermediate component for convenience, resulting in the composites being non-biodegradable[2].

We are trying to put together an easy fabrication method to synthesize similar biodegradable composites which are scalable and can extend to macroscopic free-standing membranes. Lipids with their amphiphilic properties and self-assembly is a promising candidate for the fabrication of layered structures with an appropriate component. This necessitates water as the solvent component to facilitate the amphiphilic properties of lipid. However, graphene is water-insoluble and does not find water as a very suitable dispersing medium in the absence of additional surfactants. Besides, graphene also exhibits a lack of long-term stability and the tendency to self aggregate, both characteristics not suitable for a stable result. Graphene oxide-lipid interaction had been explored in the past, however, most of the studies were limited to monolayer or bilayer interaction[3] and in computation[4][5]. Few papers extended the study to composite synthesis but used sophisticated techniques like layer by layer deposition[6], Langmuir Blodgett, or quartz crystal microbalance with dissipation monitoring(QCM-D)[7] for the fabrication. Considering the vast application this combination possesses in the field of biosensing[8][9], nanosafety applications, an easy and scalable fabrication method for the composite is of significant value.

2. Materials and Methods

2.1. Graphene Oxide Synthesis

Graphene oxide was synthesized following Hummer's method[10][11]. 2.5 grams of Graphite powder (<20 microns, Sigma Aldrich Brand) was mixed with 1.25 grams $NaNO_3$. The mixture was transferred to a beaker

containing 57.5 ml of H_2SO_4 and stirred at 500 rpm with a magnetic stirrer for 10-15 minutes. The heat generated in the process was pacified by transferring the beaker to an ice bath. 7.5 grams of $KMnO_4$ was added in small quantities. During this process, the temperature of the mixture is monitored with the help of a thermostat and the temperature was prevented from rising over 30°C with the help of an ice bath. A dark green solution as obtained was stirred at 1000 rpm vigorously for 3 hours, maintaining the temperature at 35° C. The color of the solution when changed from green to brown, the mixture was further diluted with 115 ml of deionized water that was added dropwise in an ice bath to maintain the temperature below 30° C. The resultant mixture was poured into 350 ml of deionized water, followed by the immediate addition of 6ml of 30% H_2O_2 to eliminate any unreacted $KMnO_4$. A yellow tinge is developed in the solution. The mixture was stirred for 2 more hours to mix well and was left to sediment overnight. The next day, the liquid was separated from the sediment and decanted via centrifugation. The sediment, in this case, graphite oxide was further redispersed in 4% HCl solution to be centrifuged at 7600 rpm for 3 mins and decanted. 600 ml of 4% HCl solution was prepared in total to repeat the process three times(200 ml used in each step distributed into 4 of the 50 ml centrifuge tubes). Two additional stages of purification were undertaken using distilled water in the place of 4% HCl solution. The more times centrifugation is conducted with HCl and DI water, the more the purity of the end product will be. The final sediment was collected together and redispersed in 250 ml distilled water and left to sediment out overnight. The solution was then exfoliated in a probe sonicator at 120W (130 Watts true power, amplitude 93%) for 1hr at 10 sec-15 sec, on-off pulses. The sonicated solution was centrifuged for 6 min at 7600rpm to extract the supernatant, graphene oxide. To confirm the presence of graphene oxide a part of the solution was diluted 500 times and observed with UV spectroscopy. The characteristic peak of graphene oxide is 230nm[12] and the diluted solution gave a peak at 232nm indicating the presence of graphene oxide. The formation of graphene oxide was later confirmed by the XRD peak at 9.8°, implying an interplanar distance of 0.9 nm. This is close to the characteristic peak generally observed ~10-11°[13].

One set of GO was synthesized and the concentrated version was used throughout the experimentation. The concentration of graphene oxide in the prepared volume was calculated by averaging out the residue weight of multiple evaporated samples of known volumes. The concentration of the GO was obtained to be 12.6 mg/ml.

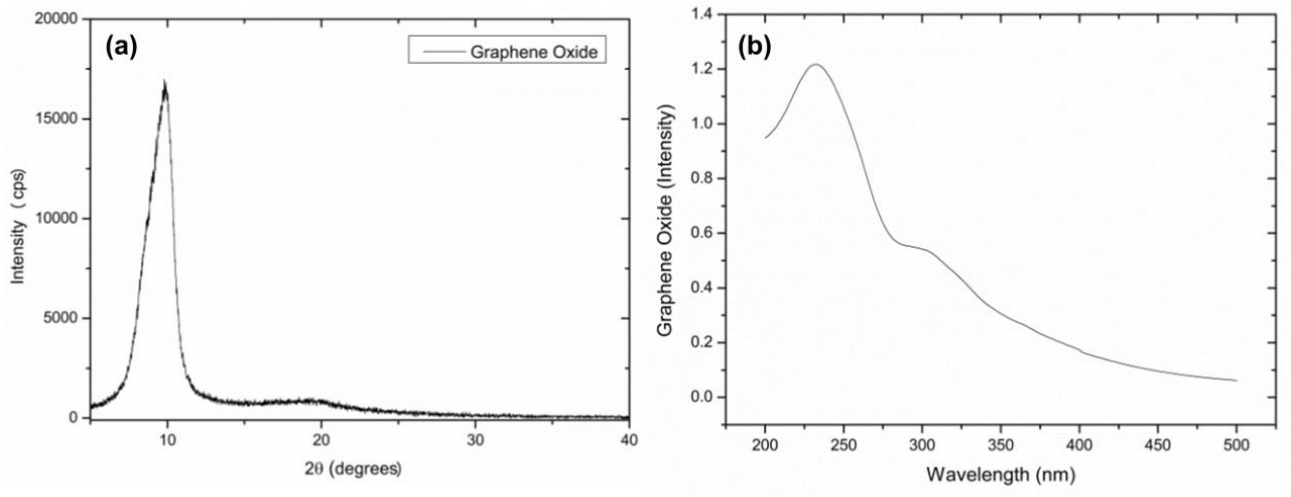

Fig 1: (a) XRD peak of graphene oxide, (b) UV-Vis peak of graphene oxide

2.2. SUV Synthesis

Small Unilamellar Vesicles (SUVs) of 1,2-dioleoyl-sn-glycero-3-phosphocholine(DOPC, powder-1G, Sigma Aldrich brand) were synthesized in the preparation of the nanocomposite. DOPC was dissolved in chloroform in 10 mg/ml concentration and the chloroform was evaporated to dryness at room temperature, spread on a petri dish. The sample was kept in a vacuum for a further six hours to remove solvent traces if any. The residue was redispersed in distilled water, maintaining the concentration at 10 mg/ml. After ensuring proper dispersion, the sample was incubated for 24 hours at 37°C. Further, the obtained lipid suspension was

sonicated using a probe-type sonicator till the solution turned clear (~5-10 mins, 30% intensity). After sonication, the solution was filtered through a 0.2μm syringe filter (Axiva brand) to form SUVs.

2.3. Sample/ Film Preparation

GO-DOPC nanocomposite films were prepared by drop-casting the sample followed by incubation evaporation. Liquid samples of various GO: DOPC proportions were synthesized by vortex stirring the appropriate amount of GO suspension and SUVs. Simple glass substrate was used for initial drop-casting. The appropriate cut square glass substrates were previously probe sonicated in a soap solution, K_2Cr_2O7, acetone, and DI water for 5 mins each with intermediate DI water rinsing. The substrates were chosen according to the sample sizes suiting various instruments of characterization. While atmospheric drying and vacuum filtration of the liquid samples consumed long hours but gave homogenous sheets, rapid drying in a vacuum oven was accompanied by multiple bubble formations resulting in uneven samples with hollow pockets. The optimum conditions were achieved on drying the samples in an incubator at 37°C. This offered the sample sufficient time to dry uniformly and at the same time never consumed more than a few hours depending on the sample size. This method offered flexibility in terms of the size and shape of sample preparation as we shifted to using 3D printed molds accurately fitting various testing samples. The base of the molds used for incubation was generally covered with parafilm for ease of peeling the final films formed. 10 ml of sample approximately yielded a 0.1mm thick circular film of 2 cm radius. These films exhibited a homogeneous morphology under the inspection of a Scanning Electron Microscope.

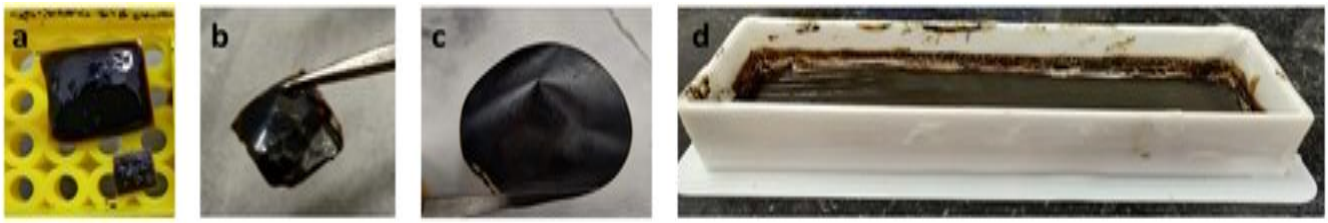

Fig 2: (a) Drop cast samples, (b)Dried and Peeled off, (c)Vacuum Filtered sample,(d) Mould drying in the incubator

3. Results and Observations

The free-standing membranes synthesized of graphene oxide-lipid composite were inspected for their morphology using a scanning electron microscope (SEM: JSM7600F (Jeol) model, resolution: 1.0 nm(15 kV), 1.5 nm(1 kV), magnification: 25x to 1,000,000x). The layered structure as observed was analyzed further to understand the impact of the addition of DOPC SUVs to GO using X-Ray Diffraction(Multipurpose XRD: Rigaku SmartLab model with a Rotating Anode X-ray Source of 9KW Output Power) results. The XRD peaks obtained were then used to calculate the average number of layers formed of the composite contributing to the results. These membranes were further tested for their chemical stability and thermal stability (Thermogravimetric Analyzer, Perkin Elmer TGA 4000). Finally, the mechanical properties of the composites were inspected using a Dynamic Mechanical Analyser (Perkin Elmer: DMA 8000 with Rotating Analysis Head, 120-160 VAC, 50-60 Hz) to obtain their storage and loss modulus. Tensile tests (Shimadzu, Japan AG-IS Universal Testing Machine, Range 0-50 kN, Accuracy 0.1 N) were additionally performed to obtain their tensile modulus and toughness.

3.1. Scanning Electron Microscopy

SEM images of GO from the top show that GO exhibits a layer-by-layer stacked structure (Fig.3). Further, the synthesized GO-DOPC composite was inspected under SEM to obtain a similar layered structure (Fig.3) to that of Graphene oxide. Hence, DOPC does not seem to alter the layers of GO in the composite, which eventually resembles the brick and mortar arrangement in the nacre shell structure as desired. However, further clarity on graphene oxide-lipid arrangement and design could only be provided after further study on the interlayer separation of different GO-DOPC combinations. This is achieved through XRD measurements.

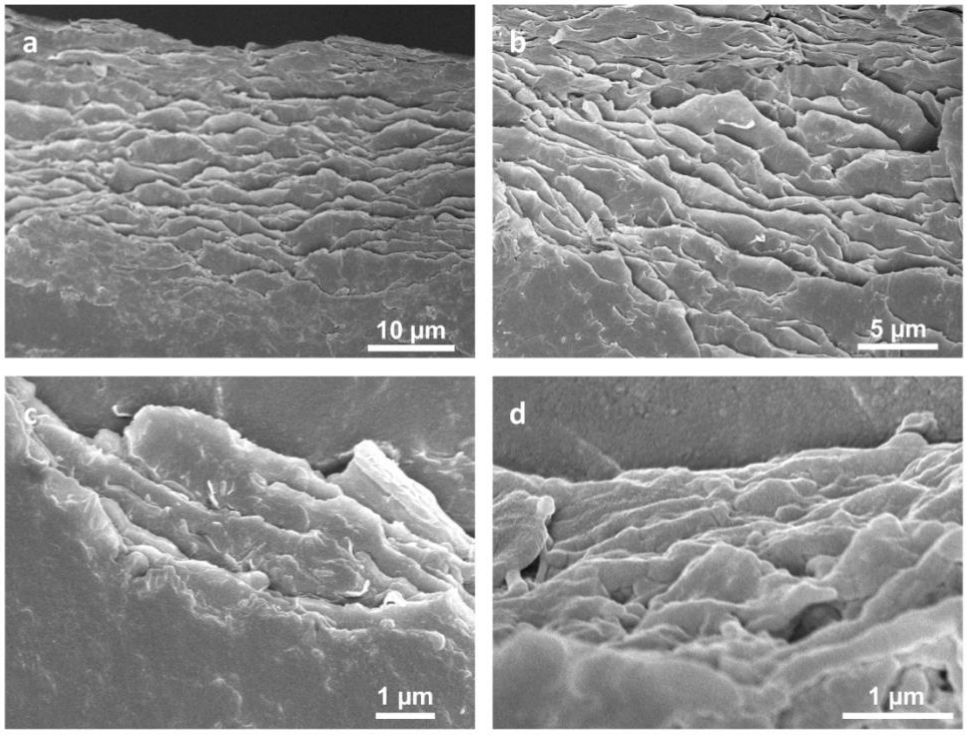

Fig 3: Layered Structure of GO at 15º tilt(top), GO-DOPC composite at 25º tilt(bottom left) and top view(bottom right)

3.2. X-Ray Diffraction

The GO: DOPC liquid samples were prepared in 8:2, 7:3, 5:5, and 2:8 proportions and separately drop cast and dried in 10mm x 10mm substrate sizes. Grazing Incidence X-ray Diffraction (GIXRD) analysis was performed on these samples at an incident angle of 1º and a 2θ range of 5º-40º. The results plotted (Fig.4) are after subtraction of background data from the glass substrate. While the GO peak was around 9.8º, introducing 20%, 30%, 50%, and 80% of lipid into GO respectively gave peaks at 9.1º, 8.58º, 8.74º, and 8.32º. The result exhibited a clear shift in the peaks that duly represent an increase in the lamellar spacing with increasing lipid proportion. This proves the intercalation of lipid molecules between the graphene oxide sheets. It was clearly observed that as the concentration of lipids rises in the mixture, the graphene oxide undergoes a respective expansion between the sheets but still maintains the layers of its structure as observed from SEM results.

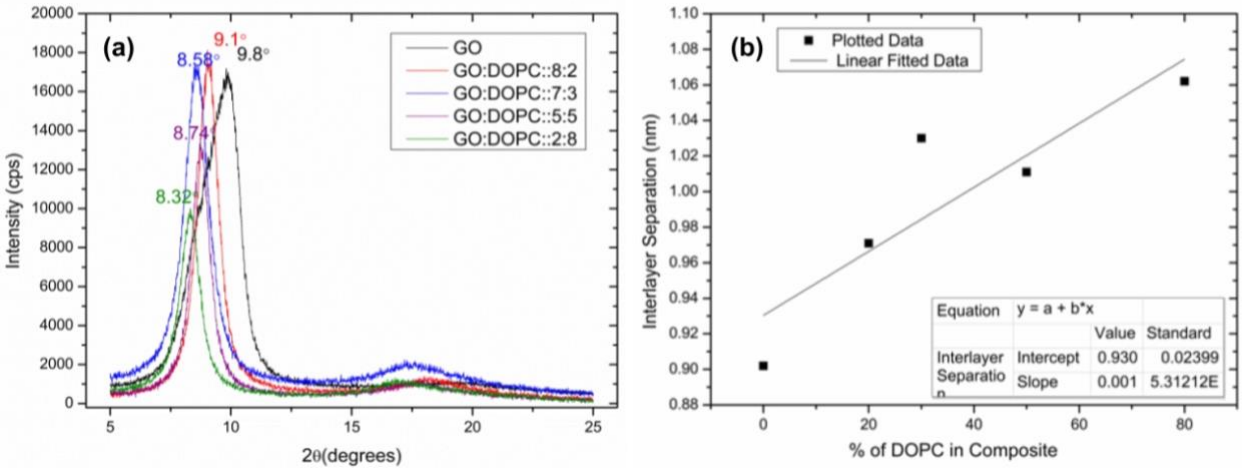

Fig 4: (a)XRD peaks of GO and GO: DOPC composite in various proportions,
(b) Calculated interlayer separation plotted against DOPC % in the composite

XRD peak profiles were further analyzed to obtain information about the number of layers stacked in these structures[14]. The prominent peak obtained from the GO: DOPC composites were cropped and fit to obtain the full width at half maxima(FWHM) Using FWHM (λ) and a shape factor, k of 0.89 which corresponds to spherical crystals with cubic unit cells, the average crystallite width (D) and in-plane crystallite size (L) were calculated according to Scherrer's formula.

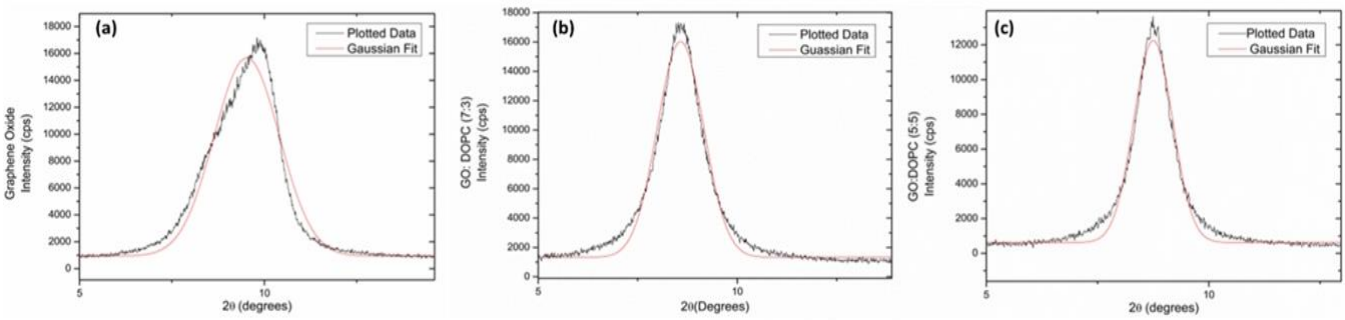

Fig 5: Gaussian Fitted XRD graphs of (a)GO and GO: DOPC composite in (b)7:3 and (c)5:5 proportions

While Bragg's equation was used earlier to calculate the interplanar distance(d) from θ corresponding to the resultant peaks, a combination of Bragg's equation and Scherrer's formula was further used to calculate the number of layers (n).

$$D = \frac{k\lambda}{\beta\, cos\theta} \tag{1}$$

$$L = \frac{k\lambda}{\beta\, cos\theta} \tag{2}$$

$$n = \frac{D}{d} + 1 = \frac{2k\, tan\theta}{\beta} + 1 \tag{3}$$

Table 1: Number of Layers calculated for the samples using Scherrer's and Bragg's equations

Sample	2θ	Interplanar Distance (d)	FWHM(λ)	Crystallite width(D)	In-plane Crystallite Size (L)	Number of layers(n)
GO	9.5°	9.3 A°	2.077° → 0.03625 rad	37.9547 A°	78.468 A°	5.08 ~ 5
GO: DOPC (5:5)	8.71°	10.14 A°	1.063837°→ 0.018567 rad	73.84666 A°	153.11 A°	8.319 ~ 8
GO: DOPC (7:3)	8.57°	10.31 A°	1.3683°→ 0.02388 rad	57.57862 A°	119.039 A°	6.68 ~ 7

The results showed the number of layers stacked contributing to the structure as obtained in the XRD results to be approximately 5 in graphene oxide and 7-8 in the composite.

3.3. Chemical and Thermal Stability

The fabricated membranes were tested for their stability in solvents capable of individual dissolution of the constituents. Small-square pieces of GO and GO: DOPC sheets were immersed in both water and chloroform to check their eventual solubility in these solvents. The composite exhibited good stability in both the solvents as they stayed insoluble in both chloroform and water for a period of 60 days.

Further, thermogravimetric analysis was performed to observe the thermal stability of the composite with respect to graphene oxide. Analysis was performed in the air medium with a flow rate of 20 ml/min. The

samples were taken to 900°C starting from room temperature. GO underwent the first decomposition around ~200°C, the same being straight reflected in the composite. This could be attributed to the carboxylic decomposition of the various groups attached to graphene oxide[15]. The second decomposition of GO at 650°C was however delayed by lipids causing the composite to eventually decompose at 900°C. The composite hence shows satisfactory thermal stability, as compared to the GO constituent and in fact, shows an improvement in thermal stability is observed with the addition of lipids.

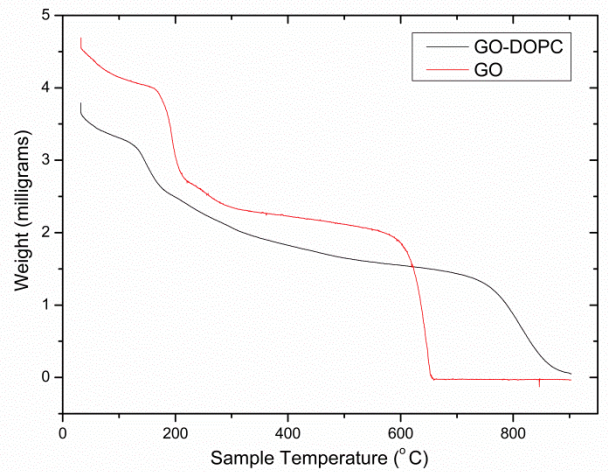

Fig 6: TGA graphs plotted to compare GO and GO: DOPC decomposition

3.4. Dynamic Mechanical Analysis

Tensile test analysis was carried out using Dynamic Mechanical Analyser in constant strain mode on the composite membranes. The loss modulus and storage modulus values of the composite stood up to be comparable to graphene oxide and their past reported values. The sample quality had a huge role to play in the test results as a more homogenous and uniform sample gave better results and was considered to be more close to the exact results. This leaves a potential for further improvement in the event of a better sample preparation method.

Table 2: Number of Layers calculated for the samples using Scherrer's and Bragg's equations

Sample	Storage Modulus @1 Hz	Storage Modulus @5.5 Hz	Storage Modulus Mean	Loss Modulus @1 Hz	Loss Modulus @5.5 Hz	Loss Modulus Mean
GO	2.16868×10^9	2.5912×10^9	2.424×10^9	3.0665×10^8	3.2144×10^8	3.1525×10^8
GO: DOPC	3.1525×10^8	2.1445×10^9	1.999×10^9	2.7715×10^8	3.1532×10^8	2.985×10^8

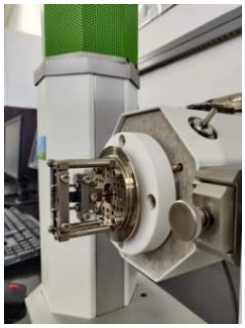

Fig 7: DMA measurements being carried out on a GO: DOPC sample

3.5. Tensile Test

Tensile testing was performed on 15cm x 1cm samples in a Universal Testing Machine to further evaluate Young's modulus, toughness, fracture stress, and strain. ASTM 3039 was followed to analyze GO: DOPC composites synthesized in two different proportions, 5:5 and 7:3. A comparison is drawn to understand the effect of lipid proportion on the mechanical properties.

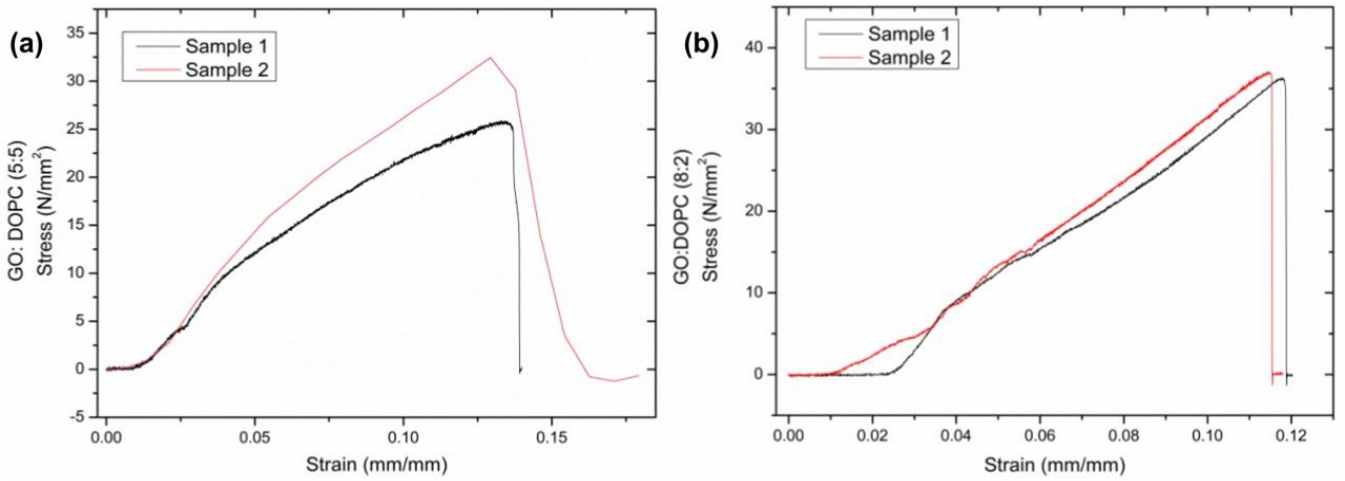

Fig 8: Stress-Strain graphs of GO: DOPC in (a)5:5 and (b)8:2 proportions

Table 3: Mechanical Properties of GO: DOPC composite from UTM Results

Sample	Young's Modulus	Toughness	Fracture Stress	Fracture Strain
GO: DOPC (5:5)	232 MPa	2.3 MPa	~27 MPa	0.14
GO: DOPC (8:2)	363 MPa	1.8 MPa	~35 MPa	0.115

An increase in strength and ductility in the composite from GO may mean that the lipid molecules are modulating the interaction between the GO sheets and this interaction is greater between the individual GO sheets. However, observed is a mild increase in toughness at the cost of modulus values in the composite as the lipid proportion increases. However, the tensile modulus values and other results obtained are far lower in magnitude than graphene oxide data.

4. Conclusion

We present an easy, scalable synthesis method established through the self-assembly of lipids to generate an alternating layer-by-layer graphene oxide-lipid composite. The composite from the liquid phase is ultimately taken into the form of macroscopic free-standing membranes that opens the possibility of doing mechanical testing on them like any tangible sheet. Having successfully intercalated lipids between the graphene oxide sheets, this serves as a biodegradable alternative to previously synthesized graphene and polymer based composites. However, the whole study accounts to only provide a preliminary synthesis method of a graphene oxide-lipid composite. The layered structure, thermal and chemical stability of the sheets are listed in the present study. The lamellar separation analysis and stacked quantity of layers reassure the quality of the composite. The mechanical side of properties is also looked upon in a basic check but not dwelled into the details. However, further research could be extended to improvements in the sample preparation and to exploring other properties left unexplored. In the future, the study can also be extended to other charged lipids and graphene itself in the place of graphene oxide.

References

[1] J. Sun and B. Bhushan, "Hierarchical structure and mechanical properties of nacre: A review," *RSC*

Adv., vol. 2, no. 20, pp. 7617–7632, 2012, doi: 10.1039/c2ra20218b.
[2] U. Khan, P. May, A. O'Neill, and J. N. Coleman, "Development of stiff, strong, yet tough composites by the addition of solvent exfoliated graphene to polyurethane," *Carbon N. Y.*, vol. 48, no. 14, pp. 4035–4041, 2010, doi: 10.1016/j.carbon.2010.07.008.
[3] L. Rui *et al.*, "Reduced graphene oxide directed self-assembly of phospholipid monolayers in liquid and gel phases," *Biochim. Biophys. Acta - Biomembr.*, vol. 1848, no. 5, pp. 1203–1211, 2015, doi: 10.1016/j.bbamem.2015.02.018.
[4] T. Rivel, S. O. Yesylevskyy, and C. Ramseyer, "Structures of single, double and triple layers of lipids adsorbed on graphene: Insights from all-atom molecular dynamics simulations," *Carbon N. Y.*, vol. 118, pp. 358–369, Jul. 2017, doi: 10.1016/j.carbon.2017.03.072.
[5] N. Willems *et al.*, "Biomimetic Phospholipid Membrane Organization on Graphene and Graphene Oxide Surfaces: A Molecular Dynamics Simulation Study," *ACS Nano*, vol. 11, no. 2, pp. 1613–1625, Feb. 2017, doi: 10.1021/acsnano.6b07352.
[6] R. Frost, G. E. Jönsson, D. Chakarov, S. Svedhem, and B. Kasemo, "Graphene oxide and lipid membranes: Interactions and nanocomposite structures," *Nano Lett.*, vol. 12, no. 7, pp. 3356–3362, Jul. 2012, doi: 10.1021/nl203107k.
[7] D. A. Melendrez, T. Jowitt, M. Iliut, A. F. Verre, S. Goodwin, and A. Vijayaraghavan, "Adsorption and binding dynamics of graphene-supported phospholipid membranes using the QCM-D technique."
[8] P. K. Ang *et al.*, "A bioelectronic platform using a graphene-lipid bilayer interface," *ACS Nano*, vol. 4, no. 12, pp. 7387–7394, Dec. 2010, doi: 10.1021/nn1022582.
[9] A. V. Titov, P. Král, and R. Pearson, "Sandwiched graphene-membrane superstructures," *ACS Nano*, vol. 4, no. 1, pp. 229–234, Jan. 2010, doi: 10.1021/nn9015778.
[10] W. S. Hummers and R. E. Offeman, "Preparation of Graphitic Oxide," 1958. Accessed: Jun. 29, 2021. [Online]. Available: https://pubs.acs.org/sharingguidelines.
[11] A. Ojha and P. Thareja, "Electrolyte induced rheological modulation of graphene oxide suspensions and its applications in adsorption," *Appl. Surf. Sci.*, vol. 435, pp. 786–798, Mar. 2018, doi: 10.1016/j.apsusc.2017.11.157.
[12] F. T. Thema *et al.*, "Synthesis and characterization of graphene thin films by chemical reduction of exfoliated and intercalated graphite oxide," *J. Chem.*, 2013, doi: 10.1155/2013/150536.
[13] J. L. S. Gascho, S. F. Costa, A. A. C. Recco, and S. H. Pezzin, "Graphene oxide films obtained by vacuum filtration: X-ray diffraction evidence of crystalline reorganization," *J. Nanomater.*, vol. 2019, 2019, doi: 10.1155/2019/5963148.
[14] A. Kaushal, S. K. Dhawan, and V. Singh, "Determination of crystallite size, number of graphene layers and defect density of graphene oxide (GO) and reduced graphene oxide (RGO)," *AIP Conf. Proc.*, vol. 2115, no. July, pp. 1–5, 2019, doi: 10.1063/1.5112945.
[15] F. Najafi and M. Rajabi, "Thermal gravity analysis for the study of stability of graphene oxide–glycine nanocomposites," *Int. Nano Lett.*, vol. 5, no. 4, pp. 187–190, 2015, doi: 10.1007/s40089-015-0154-7.

Proceedings of the SurfCoat Korea 2021 / Graphene Korea 2021 Joint Virtual International Conferences
May 26 – 28, 2021, (Held Virtually)
DOI: https://doi.org/10.26799/cp-surfcoat-graphene-korea-2021

Chloride Migration in Graphene Oxide Concrete

Boksun Kim[1], Megan Ambrose[1]

[1]University of Plymouth, School of Engineering, Computing and Mathematics, Plymouth, UK,
boksun.kim@plymouth.ac.uk

Abstract

This paper presents experimental work on the chloride penetration resistance of concrete, incorporating 0%, 2% and 3% Graphene Oxide (GO) by weight of cement. Nine 100mm diameter and 200mm high concrete cylinders were cast in the Materials Laboratory at the University of Plymouth. The cylinders were cut into 50mm thick disks and rapid chloride migration tests were carried out. After the tests, the penetration depth of the disks were measured and chloride migration coefficients were determined. It was found that compared with the control samples, the addition of 2% and 3% GO reduced the migration coefficient of concrete by about 11% and 17% respectively at 28 days after casting. This suggests that the inclusion of GO into a cementitious mix does have a noticeable effect on the increase of chloride resistance and hence the longevity of concrete.

Keywords: Graphene Oxide; Rapid Chloride Migration Test; Chloride Penetration; Chloride Migration Coefficient; Permeability; Concrete

1. Introduction

Concrete used in marine environments faces severe challenges. Traditional concrete is very brittle, which can lead to micro-cracks and void gaps. Cracks can cause serious damage to concrete structures, in particular, those exposed to coastal environments since sea salt can induce chloride ingress and allow penetration into the concrete. This chloride infiltration corrodes the steel reinforcements in the concrete. The corrosion can cause a detrimental damage to the strength, aesthetics and serviceability of structures. Hence, developing chloride resistant, durable concrete is required.

Ever since its discovery in 2004 [1], graphene has provided a new way to solve the issues that concrete faces in harsh environments due to graphene's exceptional mechanical, thermal, optical and electrical properties, and electrical conductivity. It is an ideal nano-filler that can modify the cementitious material, although it is hard to synthesize and very expensive at present. It can be synthesized to Graphene Oxide (GO): layered graphite interspersed with oxygen molecules around its plane and edges called functional groups and then exfoliated into single-layer and few-layer GO sheets. Addition of a small amount of graphene into a concrete mix can significantly improve the strength of concrete [2-7].

The majority of research with GO in cementitious materials deals with strength and stiffness. There is little research in the field of durability. In particular, how GO affects cementitious materials to resist harmful agents such as chlorides in water. Dimov et al. [2] carried out a sorptivity permeability test on GO concrete where specimens were left in a shallow container of water for and the height of water penetration after 7 days was measured across the surface. They found that there was a 400% reduction in penetration of the graphene concrete for a concentration of 0.8g/L graphene, compared with the standard concrete. However, the water level measured on the surface on the samples could have been different to the absorption inside the samples. This could be due to the porous nature of concrete as well as due to curing partially in the air.

Hence, a more established test is required to investigate the chloride penetration resistance of cementitious materials. This paper aims to investigate the effect that the addition of GO has on the chloride penetration resistance of concrete by conducting well-established rapid chloride migration tests [8-9].

2. Experimental Work

DOI: https://doi.org/10.26799/cp-surfcoat-graphene-korea-2021

Rapid Chloride Migration tests were carried out in the Materials Laboratory at the University of Plymouth. Nine 100mm diameter and 200mm height concrete cylinders were prepared and cast with 0%, 2% or 3% Graphene Oxide (GO) by weight of cement.

Water and single layer of GO (an average of 1.3 μm equivalent diameter) were split into equal amounts in small narrow containers, as shown in Figure 1 (a). They were suitably sized for the ultrasonic prop in Figure 1 (b) to be effective. Each water-GO mixture was ultra-sonicated for 1 minute at 16 Hz, stopped for 15 seconds and then ultra-sonicated for a further minute. All water-GO mixtures were emptied into a large bowl or a concrete mixer and mixed for one minute before polycarboxylate ether superplasticiser was added and further mixed for one minute to help the dispersion of the GO flakes.

The cylinders were cast using 1 part of CEM1 Portland Cement, 1.44 parts of sand, 1.76 parts of coarse aggregates with the maximum size of 10 mm, a water-cement ratio of 0.6 and 1 % superplasticiser by weight of cement. The cylinders were cast and stored at room temperature for 3 days before being removed from their moulds and placed in a water bath at 24°C where they remained for a further 24 days.

A day before testing, the cylinders were removed from the water bath and immediately weighed in air and in a water bath to obtain the density. The cylinders were cut into 50mm deep disks using a water-cooled diamond-edged saw blade. The two middle, B and T (B for bottom and T for Top. See Figure 2 (a) for locations) disks were tested at 28 and 29 days after casting.

Rapid Chloride Migration (RCM) tests were carried out using Nordtest Method NT BUILD 492 [8] to measure the penetration depths along the disks and then calculate their chloride migration coefficients. Three disks were placed at one time in a vacuum chamber, as shown in Figure 2 (b) with a pressure of 0.95 bars for 3 hours. The disks were then submerged in a calcium hydroxide solution under the same vacuum condition, as shown in Figure 2 (c) and left for 1 hour. The vacuum chamber was then released, and samples were left submerged for 18 further hours. After the preconditioning, the disks were placed in the RCM test set up, as shown in Figure 2 (d) and had an initial voltage of 30 V applied to read the current.

At the end of each RCM test, each of the disks were spilt from top to bottom through the centre, using a hammer and chisel and sprayed with a silver nitrate solution under a ventilation hood to measure the chloride penetration depths. Figure 2 (e) shows an example of the measurement.

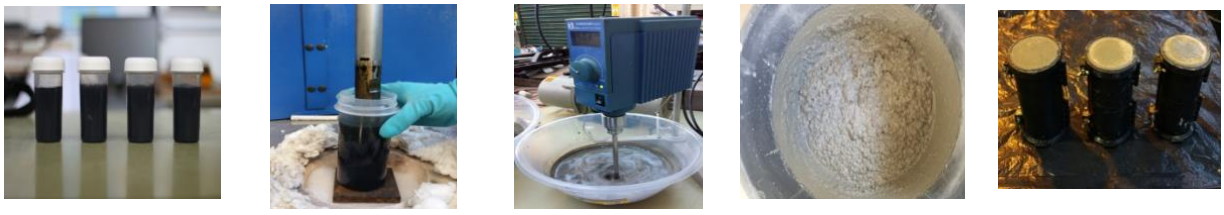

(a) (b) (c) (d) (e)

Fig. 1: Dispersion of GO in water and casting. (a) GO in water; (b) Ultra-sonicating GO; (c) Adding cement into GO and water mixture; (d) Concrete mixing; (e) Casting cylinders

(a) (b) (c) (d) (e)

Fig. 2: Rapid Chloride Migration tests: (a) Locations of disks; (b) Layout of concrete disks in vacuum chamber; (c) CaOH2 solutions submerging the disks; (d) Disks placed in reservoir ready for testing; (e) Measuring the penetration depth of a concrete disk

Proceedings of the SurfCoat Korea 2021 / Graphene Korea 2021 Joint Virtual International Conferences
May 26 – 28, 2021, (Held Virtually)
DOI: https://doi.org/10.26799/cp-surfcoat-graphene-korea-2021

3. Results and Discussion

Figure 3 shows the penetration depths along the concrete disks. As the amount of GO increased, the penetration depth decreased. The reduction is as much as 13% and 11% when 2% and 3% of GO was added respectively. The latter had a lower reduction than the former because Disks T1 and T2 had unusually large readings at D7 and D3 respectively, as shown in Figure 3 (c).

The Non-Steady-State Migration Coefficient, Dnssm ($x10^{-12}m^2/s$) for each disk was calculated using the equation below [8]:

$$Dnssm = \frac{0.0239(273+T)L}{(U-2)t}\left(X_d - 0.0238\sqrt{\frac{(273+T)L*X_d}{U-2}}\right) \quad (1)$$

Where U is the absolute value of the applied voltage (V); T is the average value of the initial and final temperature in the anolyte solution (°C); L is the thickness of specimen (mm); X_d is the average value of the penetration depths (mm); t is test duration (hours).

The migration coefficients of the concrete disks are presented in Figure 4 (a). The effect of the inclusion of GO on the disks is shown in Figure 4 (b). The higher amount of GO, the smaller migration coefficient. Hence, compared with the control samples, the migration coefficients were reduced as much as about 10.64% and 16.61% when 2% and 3% GO was included respectively, as shown in Figure 4 (b).

The densities of the concrete cylinders were calculated using the Archimedes principle. As expected, the addition of GO increased the densities of the cylinders. The increases are as much as 0.46% and 0.83% when 2% and 3% GO were incorporated respectively, compared with their control samples.

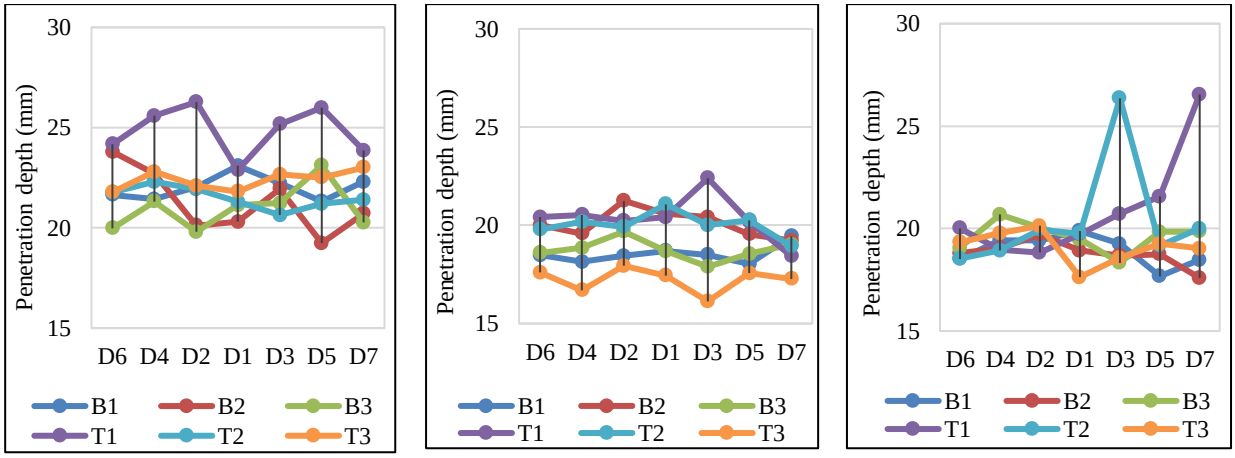

(a) 0% GO (b) 2% GO (c) 3% GO

Fig. 3: Penetration depths (T and B were tested at 28 and 29 days)

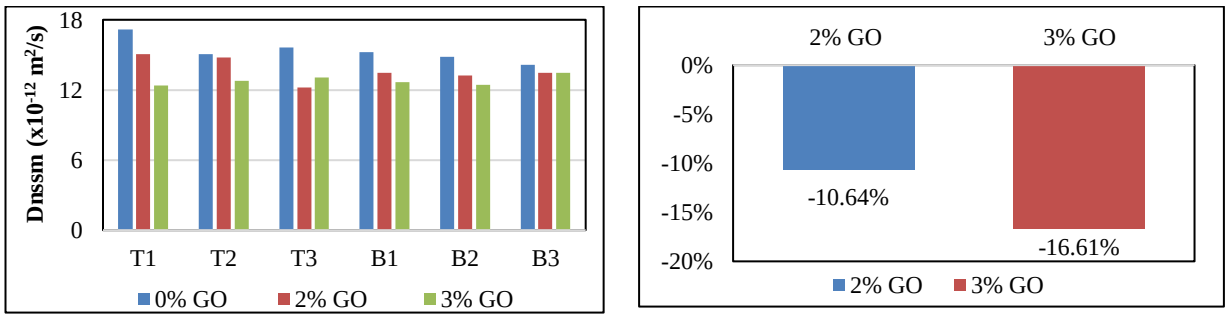

(a) Migration coefficient of concrete (T and B were tested at 28 and 29 days)

(b) Reduction of the migration coefficient of concrete

Fig. 4: Comparison of Migration Coefficient

DOI: https://doi.org/10.26799/cp-surfcoat-graphene-korea-2021

4. Conclusions

Rapid chloride migration and water absorption tests were carried out using nine 100mm diameter and 200mm high cylinders to determine the effect of 2% and 3% GO by weight of cement on the permeability of concrete. As the amount of GO increased, the penetration depth of chloride ions in the concrete samples decreased. Hence, the higher amount of GO, the smaller migration coefficient. Compared with the control samples, the addition of 2% and 3% GO reduced the migration coefficient of the concrete by about 11% and 17% respectively at 28 days after casting. This suggests that the inclusion of GO into a cementitious mix does have a noticeable effect on the increase of chloride resistance and hence the longevity of concrete.

References

1. K. Novoselov, A. Geim, S. Morozov, D. Jiang, Y. Zhang, S. Dubonos, I. Gregorieva and A. Firsov, "Electric Field Effect in Atomically Thin Carbon Films," *Science*, vol. 306 no. 5696, pp.666-669, 2004
2. D. Dimov, I. Amit, O. Gorrie, M. Barnes, N. Townsend, A. Neves, F. Withers, S. Russo and M. Craciun, "Ultrahigh Performance Nanoengineered Graphene-Concrete Composites for Multifunctional Applications," *Advanced Functional Materials*, vol. 28, no. 23, 1705183, 2018.
3. B. Kim, L. Taylor, A. Troy, M. McArthur and M. Ptaszynska, "The effects of Graphene Oxide flakes on the mechanical properties of cement mortar," *Computers and Concrete*, vol. 21 no. 3, pp.261-267, 2018.
4. T. Tong, Z. Fan, Q. Liu, S. Wang, S. Tan. and Q. Yu, "Investigation of the effects of graphene and graphene oxide nanoplatelets on the micro- and macro-properties of cementitious materials," *Construction and Building Materials*, vol. 106, pp.102-114, 2016.
5. F. Babak, H. Abolfazl, R. Alimorad and G. Parviz, "Preparation and Mechanical Properties of Graphene Oxide: Cement Nanocomposites," *The Scientific World Journal*, vol. 2014, pp.1-10, 2014.
6. X. Li, A. Korayem, C. Li, Y. Liu, H. He, J. Sanjayan and W. Duan, "Incorporation of graphene oxide and silica fume into cement paste: A study of dispersion and compressive strength," *Construction and Building Materials*, vol. 123, pp.327-335, 2016.
7. L. Li, Z. Lu, S. Chuah, W. Li, Y. Liu, W. Duan and Z. Li, "Effects of graphene oxide aggregates on hydration degree, sorptivity, and tensile splitting strength of cement paste," *Composites Part A: Applied Science and Manufacturing*, vol. 100, pp.1-8, 2017.
8. NORDTEST, "Cement-Based Repair Materials: Chloride migration coefficient from non-steady-state migration experiments," *Nordtest Method NT Build*, Vol. 492, 1999.
9. L. Tang and H. Sørensen, "Precision of the Nordic test methods for measuring the chloride diffusion/migration coefficients of concrete," *Materials and Structures*, vol. 34, no. 8, pp.479-485, 2001.